Honors College Thesis
Submitted in partial fulfillment of the requirements for graduation from the Honors College

Accelerated Discovery and Characterization of High-Temperature Superconductors Using Machine Learning, Generative Models, and Solid-State Synthesis

Edward Jansen
Dr. Ivan Fabe Dempsey Hyatt
Dr. Matthew Wright, Dr. Niraj Aryal
May 9th, 2025

Table of Contents

Abstract

High-temperature superconductivity remains one of the most compelling unsolved phenomena in condensed matter physics. Despite decades of research, a complete theoretical understanding of the pairing mechanism in high-T_c materials is still lacking. A data-driven, AI-assisted framework is proposed for discovering new high-temperature superconductors using generative models and graph-based machine learning. By training the Crystal Diffusion Variational Autoencoder (CDVAE) on known superconductor structures and critical temperatures, we generate new candidate materials optimized for stability and superconducting potential. These are screened using the Atomistic Line Graph Neural Network (ALIGNN) for thermodynamic viability and band gap predictions. Select candidates are synthesized via solid-state reactions and tested experimentally using magnetic susceptibility, resistivity, and iodometric titration to determine oxygen content. Our proposed method demonstrates how machine learning can be an effective tool to accelerate superconductor discovery, by integrating structure-property relationships, physics-informed design, and experimental feedback. This workflow represents a step toward overcoming theoretical limitations by leveraging high-dimensional data and iterative model improvement.

Chapter 1 – Introduction

What is Superconductivity?

Superconductors are materials that exhibit unique properties when cooled below a critical temperature (T_c): superconductors exhibit zero electrical resistance. Conventional conductors, for instance a copper wire, has an internal resistance. When this copper wire carries an electrical current, the resistance causes dissipation of energy due to heat. Since superconductors have no resistance, they lose no energy. Superconductors are also powerful magnets, producing a diamagnetic field upon cooling. This magnetic phenomenon is known as the Meissner Effect.

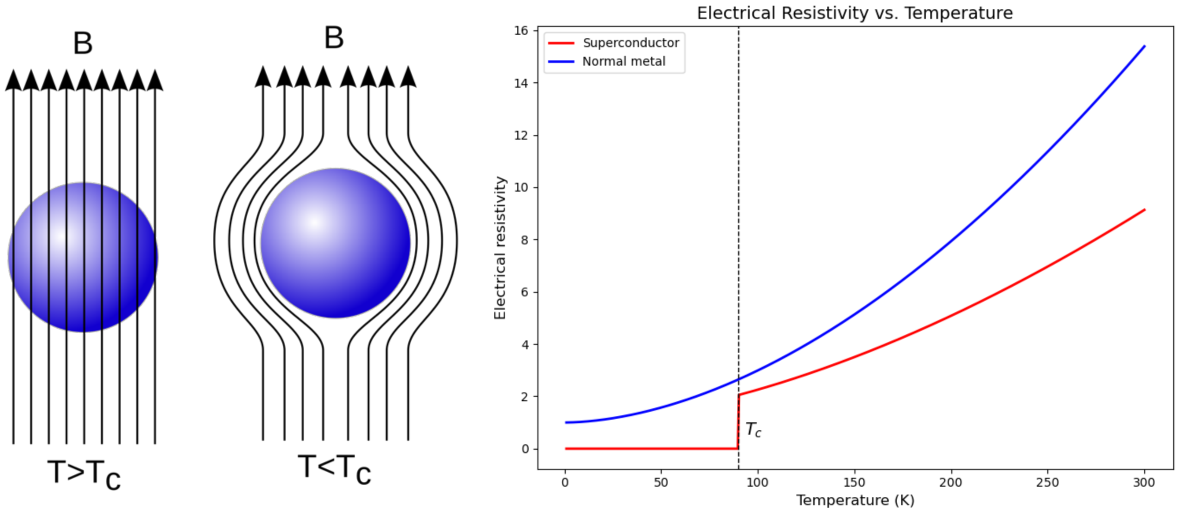

*Figure 1-1, **Left**: Visualization of the Meissner Effect. **Right**: Plot showing temperature vs. resistivity ($\rho = \frac{RA}{L}$) for conventional metal conductors and for superconductors.*

Superconductivity was first discovered in 1911 by Heike Kamerlingh Onnes, who observed that mercury cooled with liquid helium to 4 K (-296 ˚C, -452 ˚F) exhibited no resistance to electrical current.[1] The next half-century would be spent trying to explain this phenomenon. During the 1930s, the London equations were developed, relating the current of a superconductor to its electromagnetic field by analogues of Ohm's Law.[2]

$$E = \frac{\partial}{\partial t}(\Lambda \boldsymbol{J}_s) \tag{1.1}$$

$$h = -c\nabla \times \Lambda \boldsymbol{J}_s \tag{1.2}$$

For $\Lambda = \frac{4\pi\lambda^2}{c^2} = \frac{m}{n_s e^2}$, where n_s is the number density of superconducting electrons (see *Appendix*).

The next breakthrough in superconductivity—Bardeen-Cooper-Schrieffer (BCS) Theory—was Nobel Prize worthy (1972).[3] Ginzburg-Landau and Eliashberg theory expanded on this. At this point in history, superconductors were mostly single-element crystals (i.e. Pb, Al, Nb, etc.) or metal-alloys (Nb_3Sn, Nb_3Ge) that operated at or below 30 K (-243 ˚C, -406 ˚F). These temperatures were only achievable with expensive, liquid helium.[4] These temperatures are now accessible through advanced cryogenic cooling techniques.

In the 1980s the first *high-temperature* superconductor—$La_{1.85}Ba_{0.15}Cu_2O_4$ (LBCO)—was discovered in a laboratory at IBM.[5] "High-temperature", when referring to superconductors, is relative: LBCO had a superconducting critical temperature (T_c) of 35K (-238˚C, -397˚F), the highest T_c of the time. A university laboratory changed the stoichiometry and substituted lanthanum with yttrium, synthesizing $YBa_2Cu_3O_{7-\delta}$ (YBCO, T_c = 93 K, -180˚C, -292˚F).[6] YBCO was a revolutionary compound, as it was the first compound with achievable superconductivity above the boiling point of liquid nitrogen (LN2, 77 K, -196˚C, -321˚F). Liquid nitrogen is far cheaper than liquid helium[7,8] with a boiling point of 4 K, thus paving the way for an era of new technologies and applications powered by high temperature superconductors.

Superconductors vary widely in their properties, with differences in structure, composition, and the mechanisms underlying their superconducting behavior. Low temperature superconductors (LTS) can be explained by BCS theory,[3] which describes the formation of Cooper pairs, a bound state of two electrons near the Fermi level.

High temperature superconductors (HTS) do not exhibit the same electron-phonon interaction found in LTS. Theories have been proposed as to Cooper pair formation in HTS but no unifying framework exists yet.[9] Structural differences between isotropic LTSs and anisotropic HTSs suggest that HTS systems exhibit d-wave Cooper pairing, while known LTS compounds exhibit s-wave pairing.[10] In the simplest terms possible, this means that in LTS compounds Cooper pairs form equally in all directions. In HTS compounds, Cooper pairs prefer the x-y plane over propagation in the z axis.

Evidence for this exists through the superconducting coherence length, ξ_0, developed by Pippard,[11] which describes the average length for which Cooper pairs travel—the average distance that the electrons remain bound while traveling in the lattice.

$$\xi_0 = a\frac{\hbar v_F}{k_B T_c} \tag{1.3}$$

Where a is a numerical constant, $\hbar$ is Planck's constant, v_F is the Fermi velocity, and k_B is the Boltzmann constant.

Pippard proposed ξ_0 as an analog to conventional conductors, which have a quantity known as the mean free length, *l*. The mean free length describes the average length electrons travel before scattering in the lattice. At a microscopic level, this scattering causes resistance. In HTS layered, anisotropic systems, ξ_0 has been measured to be longer in the planar directions than in the axial direction (*Figure 1-2*).

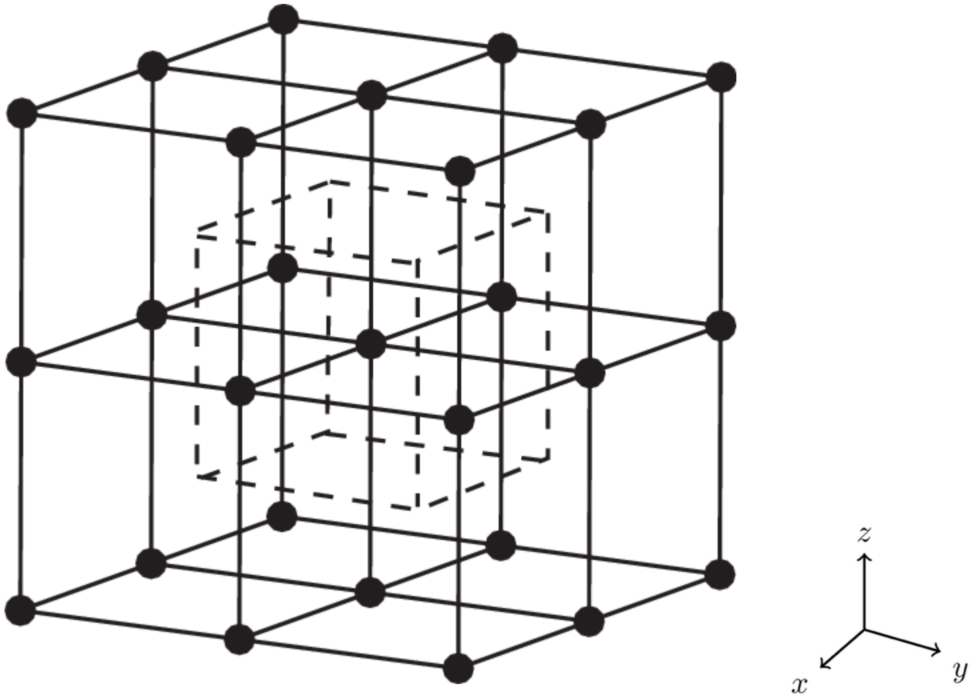

Figure 1-2. *Diagram of a simple cubic lattice structure—an example to help the reader interpret the geometry of solid-state structures, the xy plane (horizontal) and z axis (vertical).*

Despite nearly half a century since the discovery of high-temperature superconductors, no verified theory exists to explain how the underlying physics.

Applications of Superconductors

Understanding the practical applications and market potential of superconductors reveals both the transformative value and the persistent limitations of these materials. Over the past several decades, two sectors have dominated superconductor use: federally funded laboratories—particularly in particle accelerators and fusion reactors—and the medical industry, most notably for magnetic resonance imaging (MRI).[12]

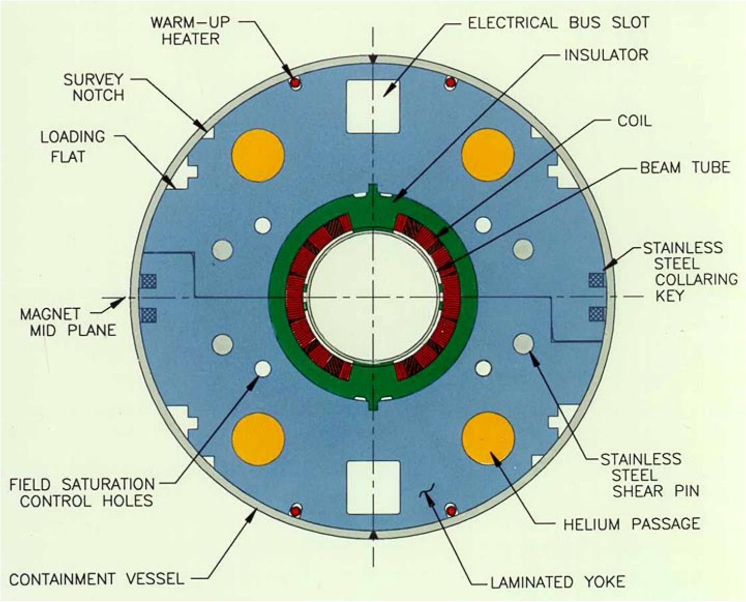

Figure 1-3. *Schematic of superconducting magnet used in the Relativistic Heavy Ion Collider (RHIC) at Brookhaven National Laboratory (BNL) on Long Island, NY.*[13]

In fusion energy research, superconductors are essential for generating and maintaining the high-field magnets used in confinement systems, as well as for advanced detection instrumentation.[14] Superconducting wires, especially low-temperature variants such as NbTi, are heavily employed in these systems. Superconductors also play a central role in Superconducting Magnetic Energy Storage (SMES) systems, which offer near-lossless energy storage when cryogenically cooled.

The use of superconductors in power transmission is feasible but limited by economic considerations.[15] The cost is not in cooling, but in the expense of converting superconducting direct current (DC) lines into alternating current (AC) grid systems. Superconducting power lines are only practical for long-distance, high-capacity routes, that require fewer conversion junctions.[12]

Transportation can also be revolutionized by superconductors, which power magnetic levitation (maglev) technology, such as maglev trains.[16] These systems, developed in the U.S. during the 1970s and widely adopted in Japan, utilize high-temperature superconductors (HTS) cooled at the base of the train. The train levitates approximately 6–10 inches above a U-shaped aluminum guideway, enabling near-frictionless, high-speed travel with low emissions and reduced mechanical wear.

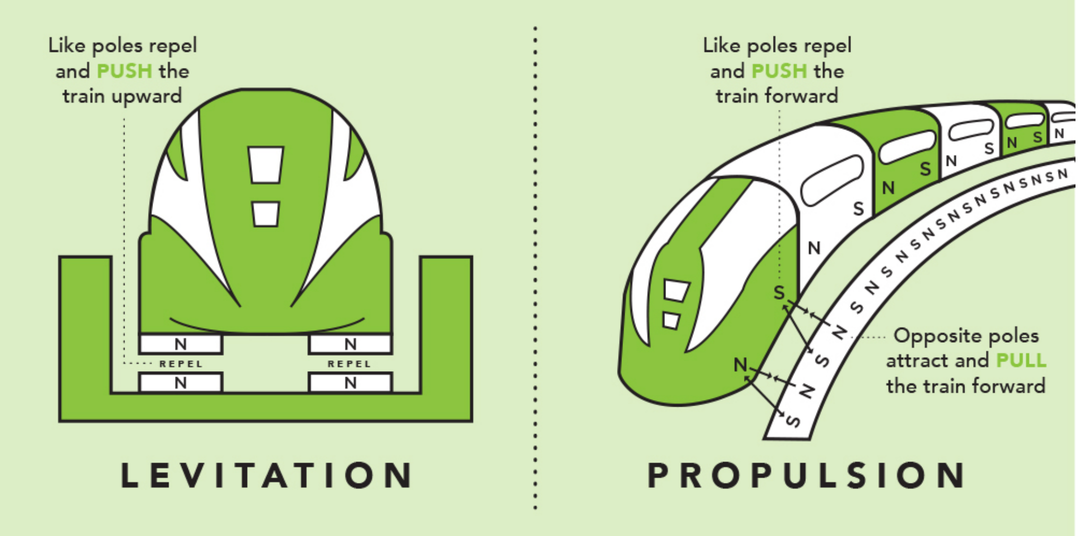

Figure 1-4. Magnetic levitation track mechanism used for high-speed rails, sourced from doe.gov..

Although the U.S. has yet to implement such systems, the proposed Northeast Maglev project aims to build the first superconducting maglev line in the country, connecting Manhattan and Washington, D.C.

Figure 1-5. Advertisement for the Northeast Maglev project, a proposed high-speed railway powered by high-temperature superconducting magnetic levitation.[17]

In electronics and computing, superconductors can create switches that operate at extremely high speeds with minimal energy loss, using quantum tunneling of Cooper pairs across Josephson junctions.[18, 19] Superconducting Quantum Interference Devices (SQUIDs) are among the most sensitive instruments for measuring magnetic fields, currents, voltages, and temperature changes. While both low- and high-temperature superconductors can be used in SQUIDs, HTS variants are often favored in applied settings due to reduced sensitivity to ambient noise and more manageable cooling requirements.[20]

Other emerging applications include superconducting generators and motors, which offer greater efficiency than conventional machines but are only cost-effective at large scales. In small-scale applications, the cost of cooling and maintenance outweighs performance gains. Superconductors have also been explored in communication technologies, though this remains a developing sector.[21]

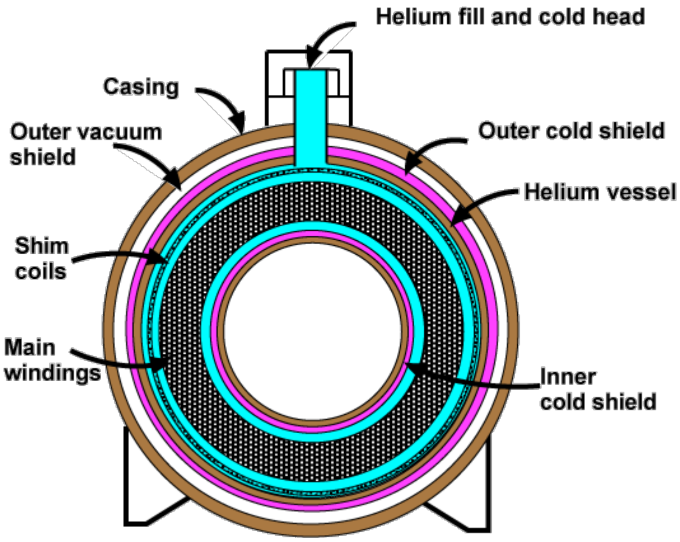

Figure 1-6. *Schematic of superconducting magnet used in MRI machines.*[22]

The most established commercial application remains medical imaging. In Magnetic Resonance Imaging (MRI), superconducting magnets generate stable, high-intensity magnetic fields used to align hydrogen nuclei in tissues. The resulting signals provide detailed anatomical and functional imaging. MRIs traditionally employ low-temperature superconducting magnets; although HTS variants offer marginal energy savings, the cost of cooling is not the primary expense, and HTS adoption in MRI systems has remained limited.[23] The global superconducting magnets market, encompassing MRI applications, is valued at USD 1.2 billion as of 2024 and projected to double over the next decade.[24]

Machine Learning in Materials Discovery

Recent advances in artificial intelligence (AI) and machine learning (ML) provide an alternative approach to discovering new materials.[25,26,27] Generative AI models accelerate the discovery of unsynthesized materials. These models do not require programming a known theory, as they are constructed to extrapolate trends from data. Models such as the Crystal Graph Convolutional Neural Network (CGCNN)[28] have provided efficient materials representations as graphs. These graphs, mathematically tensors of nodes and edges, have been pivotal in efficiently representing materials in machine learning and have paved the way for ML models to predict material properties, such as band gap, electron density of states, and formation energy, by simply being trained on structures. Data driven approaches, such as those applied in Google's Graph Networks for Materials Exploration (GNoME)[29], use ML to quickly filter which materials need further investigation by more expensive, longer DFT calculations. GNoME and others[30,31,32,33] have discovered new superconductors by this method.

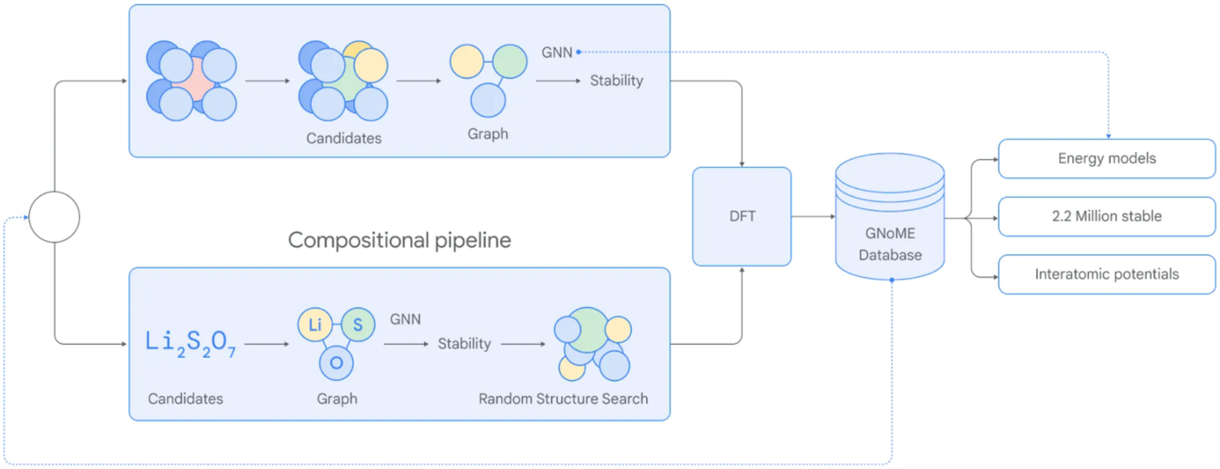

Figure 1-7. Machine learning workflow proposed by Google for the GNoME materials exploration project.

Existing materials discovery and screening pipelines leverage existing data from large datasets[34,35] as a basis to generate new material structures and compositions, filter through them quickly with ML for materials of interest, perform DFT to support those claims, and declare these new theoretical materials. Some projects take this further into experimental validation.[36,37]

Materials Project[34] is the standard hub as a crystal database, including both its own data and data contributed from other materials datasets, including the inorganic crystal structure database (ICSD)[35] for experimentally validated materials. Materials Project provides data on both experimentally validated structures and theoretically predicted DFT structures, with an easy-to-use API in Python for filtering through and downloading CIF files by programmable criteria. Filtering can be performed to favor experimentally determined crystals, a specific band gap range, or elemental composition, for instance. Each material is represented by a material-ID. Documentation and citations for each material-ID is easily accessible.

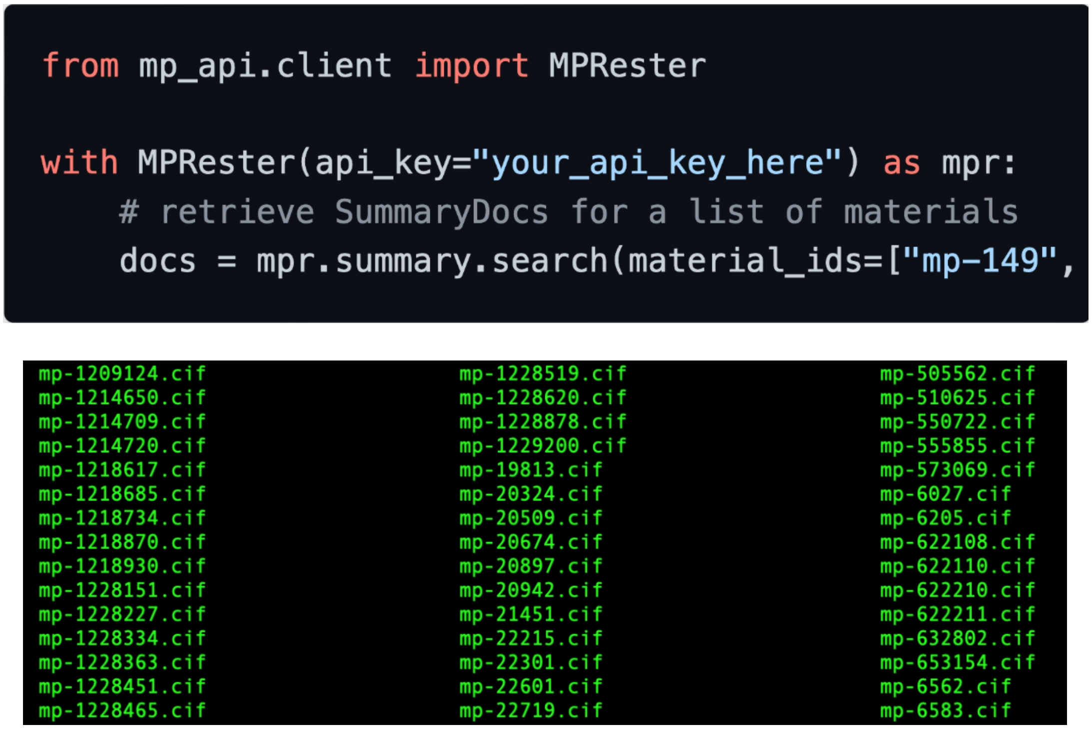

```python
from mp_api.client import MPRester

with MPRester(api_key="your_api_key_here") as mpr:
    # retrieve SummaryDocs for a list of materials
    docs = mpr.summary.search(material_ids=["mp-149",
```

```
mp-1209124.cif                    mp-1228519.cif                    mp-505562.cif
mp-1214650.cif                    mp-1228620.cif                    mp-510625.cif
mp-1214709.cif                    mp-1228878.cif                    mp-550722.cif
mp-1214720.cif                    mp-1229200.cif                    mp-555855.cif
mp-1218617.cif                    mp-19813.cif                      mp-573069.cif
mp-1218685.cif                    mp-20324.cif                      mp-6027.cif
mp-1218734.cif                    mp-20509.cif                      mp-6205.cif
mp-1218870.cif                    mp-20674.cif                      mp-622108.cif
mp-1218930.cif                    mp-20897.cif                      mp-622110.cif
mp-1228151.cif                    mp-20942.cif                      mp-622210.cif
mp-1228227.cif                    mp-21451.cif                      mp-622211.cif
mp-1228334.cif                    mp-22215.cif                      mp-632802.cif
mp-1228363.cif                    mp-22301.cif                      mp-653154.cif
mp-1228451.cif                    mp-22601.cif                      mp-6562.cif
mp-1228465.cif                    mp-22719.cif                      mp-6583.cif
```

Figure 1-8. ***Top****: Example python code for accessing the Materials Project API.* ***Bottom****: Linux shell directory listing CIF files of material-IDs from the Materials Project database.*

Google GNoME has recently contributed some 10,000 new crystals to the Materials Project database and has provided the most successful example of a machine learning based materials workflow.[38] Google GNoME works by employing advanced graph neural networks (GNNs) to predict the stability of inorganic crystal structures. It utilizes two main pipelines: a structural pipeline that generates candidates resembling known crystals, and a compositional pipeline that explores new chemical formulas. These candidates are evaluated using Density Functional Theory (DFT) calculations, and the results inform subsequent rounds of active learning. Through this iterative process, GNoME has identified over 2.2 million new crystal structures, including 380,000 predicted to be stable, significantly expanding the known landscape of stable materials. Experimental validation of AI-predicted materials lags far behind generation, as platforms like GNoME only release theoretical structures, leaving time-consuming X-ray diffraction and synthesis to external research groups.

Chapter 2 – High-Temperature Superconductivity

Current Theories & Challenges

Although high-temperature superconductivity was discovered over half a century ago, a universally accepted and experimentally validated theory describing its mechanism remains elusive. This fundamental gap in understanding continues to pose a major challenge in the rational design of new superconducting materials.

BCS Theory

BCS theory explains superconductivity in conventional, low-temperature superconductors through the formation of Cooper pairs—bound states of two electrons that arise from an effective attractive interaction mediated by phonons, or lattice vibrations. The first passing electron polarizes the lattice by displacing positive ions. The second electron is attracted to the increased positive charge density of the temporarily displaced region.[2]

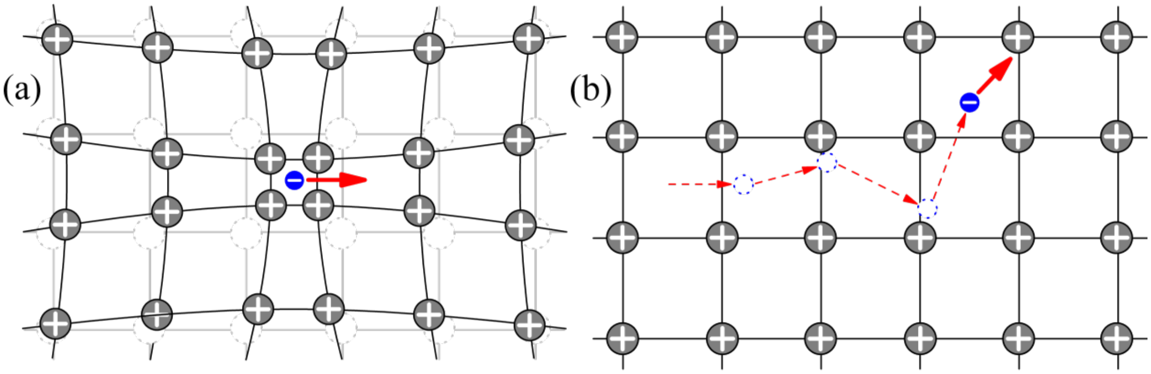

Figure 2-1. *(a) A visualization of Cooper pairs, the microscopic electron pairing mechanism proposed by BCS Theory. Lattice contractions, caused by oppositely charged traveling electrons, creates a region of temporary higher positive charge density than*

other sites in the lattice, attracting a second electron to that position. (b) A visualization of conventional resistance in a metal as the microscopic scattering of electrons off of lattice sites.[39]

According to Bloch's theorem for solids, the ground state of a periodic crystal has zero total momentum. Therefore, the lowest energy Cooper pair state consists of two electrons with opposite momenta and spin, and can be expressed by the wavefunction:

$$\psi_0(\boldsymbol{r}_1,\boldsymbol{r}_2) = \sum_{\boldsymbol{k}} g_{\boldsymbol{k}}\, e^{i\boldsymbol{k}\cdot\mathbf{r}_1} e^{-i\boldsymbol{k}\cdot\mathbf{r}_2} \tag{2.1}$$

The spin and spatial components of the wavefunction must display opposite symmetry, as this two-particle wavefunction must be antisymmetric under exchange due to the Pauli exclusion principle. ψ_0 can either follow an antisymmetric singlet spin function ($\alpha_1\beta_2$-$\beta_1\alpha_2$) or one of the symmetric triplet functions ($\alpha_1\alpha_2$, $\alpha_1\beta_2 + \beta_2\alpha_2$, $\beta_1\beta_2$), where α is spin up and β is spin down. The significance of these states is that they determine the symmetry of the superconducting order parameter. A symmetric orbital wavefunction will favor s-wave or even-parity d-wave pairing only if the spin state is the antisymmetric singlet. An antisymmetric orbital wavefunction (odd parity) is required for triplet spin states and typically results in p-wave symmetry.

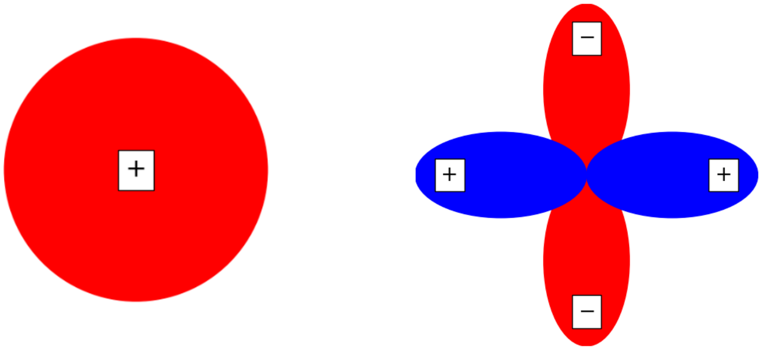

Figure 2-2. *Comparison of superconducting order parameter symmetries, s-wave (left) vs d-wave (right). s-wave pairing is isotropic and preserves full rotational symmetry, typically arising from electron-phonon interactions. In contrast, d-wave pairing exhibits fourfold symmetry with a phase that changes sign between lobes.*

The microscopic behavior of Cooper pairs is described using the BCS Hamiltonian in second-quantization:

$$H = \sum_{\vec{k},s} \xi_{\vec{k}}\ c^{\dagger}_{\vec{k}s} c_{\vec{k}s} + \sum_{\vec{k},\overrightarrow{k'},\vec{q}} V_{k,k'} c^{\dagger}_{\vec{k}+\vec{q},\uparrow} c^{\dagger}_{\overrightarrow{k'}-\vec{q},\downarrow} c_{\overrightarrow{k'}\downarrow} c_{\vec{k}\uparrow} \tag{2.2}$$

$\xi_{\vec{k}}$ is the single-particle energy measured relative to the Fermi level, and $V_{k,k'}$ is the pairing potential. This convention constructs electrons using the creation ($c^{\dagger}_{\vec{k}}$) and annihiliation ($c_{\vec{k}}$) quantum operators. Both are mathematical operators that raise (creation) or lower (annihilation) the number of particles in a given state by one.

A variational approach solves for a new quantity known as the superconducting energy gap, $\Delta_{\boldsymbol{k}}$, which represents the energy cost to excite an electron out of a Cooper pair:

$$\Delta_{\boldsymbol{k}} = -\sum_{\boldsymbol{k'}} V_{\boldsymbol{kk'}}\, u_{\boldsymbol{k'}} v_{\boldsymbol{k'}} = -\frac{1}{2}\sum_{\boldsymbol{k}} V_{\boldsymbol{kk'}}\, sin(2\theta_{\boldsymbol{k'}}) \tag{2.3}$$

The coefficients $u^2_{k'}$ and $v^2_{k'}$ represent the probabilities that a state is unoccupied or occupied, respectively, with the constraint $u^2_{k'} + v^2_{k'} = 1$.

By the Pauli exclusion principle, Cooper pairs are spin-0 bosons, composed of two ½ spin fermions (electrons). The bosonic nature of Cooper pairs allows condensation into a macroscopic quantum state described by a single wavefunction. The gap Δ defines the minimum energy required to excite particles out of this condensate and ranges within an energy window of width $\hbar\omega_c$ around the Fermi level, where ω_c is the cutoff phonon frequency (Debye frequency for metals). The energy required to excite electrons out of the Cooper pairing state must exceed this gap, and can be defined as:

$$E_k = \left(\xi_k^2 + \left|\Delta_k{}^2\right|\right)^{1/2} \tag{2.4}$$

Assuming a constant, attractive pairing interaction within energy $\hbar\omega_c$—and no Cooper pair formation outside of this range—the pairing potential is simplified to:

$$V_{kk'} = \begin{cases} -V & \text{if } |\xi_k| < \hbar\omega_c \\ 0 & otherwise \end{cases} \tag{2.5}$$

Thus, the gap, Δ, is defined as the energy range where a pairing potential is non-zero.

$$\Delta_k = \begin{cases} \Delta \text{ for } |\xi_k| < \hbar\omega_c \\ 0 \text{ for } |\xi_k| > \hbar\omega_c \end{cases} \tag{2.6}$$

BCS theory concludes that for a constant pairing potential and a constant superconducting energy gap, that Δ can be approximated as:

$$\Delta = \frac{\hbar\omega_c}{sinh[1/N(0)V]} \approx 2\hbar\omega_c e^{-1/N(0)V} \tag{2.7}$$

Where *N(0)* is the electron density of states at the Fermi level, and *V* is the magnitude of the pairing potential.

The critical temperature (T_c) for which Δ → 0, satisfies:

$$kT_c = \beta_c^{-1} = 1.13\hbar\omega_c e^{-1/N(0)V} \tag{2.8}$$

Where β_c is the thermodynamic beta at T_c. This leads to a universal relation between the zero-temperature gap and the critical temperature:

$$\Delta(0) = \Delta_0 = 1.76k_BT_c \tag{2.9}$$

Where the constant 1.76 is an experimentally verified numerical factor.

BCS theory successfully describes conventional superconductivity for materials near absolute zero. Corrections made by McMillan to (2.7) resulted in the McMillan[40] equation for critical temperature:

$$T_c = \frac{\Theta_D}{1.45} exp\left(-\frac{1.04(1+\lambda)}{\lambda - \mu^*(1+0.62\lambda)}\right) \tag{2.10}$$

Where Θ_D is the Debye temperature, λ is an experimentally determined electron-phonon coupling constant, and μ^* is the Coulomb pseuopotential. Comparing this formula's calculations of T_c for conventional superconductors with experimentally verified temperatures shows a high degree of accuracy.

Material	Experimental T_c	McMillan Predicted T_c
Lead (*Pb*)	7.19	6.48
Mercury (*Hg*)	4.19	4.51
Tin (*Sn*)	3.75	3.77

Table 1. Comparing the McMillan formula correction to BCS theory with experimentally verified values for T_c.[40]

A single unifying theory that accounts for high-temperature superconductors fails by the assumptions made for conventional, low-temperature superconductors. Theories such as Ginzburg-Landau theory and Eliashberg theory expand on BCS theory, but do not provide corrections for non LTS compounds. Calculations for the T_c of HTS compounds fail using BCS theory. The mechanism behind BCS theory relies on the phonon-mediated attraction. An alternative pairing mechanism may be needed to explain the attraction mechanism in HTS compounds.

Spin-Fluctuation Mediated Pairing

One such theory supposes that instead of phonons—quantized lattice vibrations—to mediate the attraction between electrons, magnetic fluctuations force an attraction to occur. High-temperature cuprates (copper oxide) superconductors are strongly correlated electron systems—they have electronic behaviors that cannot be described by non-interacting electrons.[41] For instance, the cuprates are antiferromagnetic insulators at room temperature. This means the electron spins on adjacent copper sites in the CuO_2 planes align in an alternating up-down pattern.

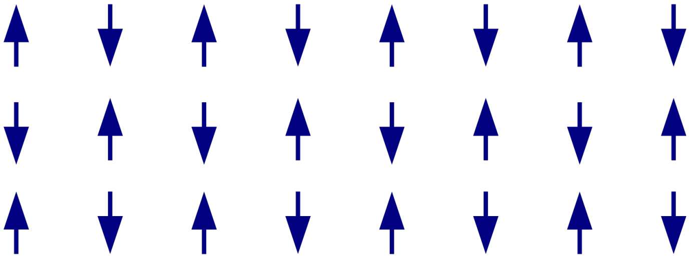

Figure 2-3. Antiferromagnetic spin ordering in the lattice.

In regions near the Fermi level, when one electron perturbs the local spin environment—such as by polarizing nearby spins—a second electron can be drawn to this disturbance. In spin-fluctuation-mediated pairing, this interaction is indirect: the repulsive Coulomb interaction between electrons is modulated by the surrounding antiferromagnetic spin background, creating an effective attraction. Though the fundamental interaction remains repulsive, the exchange of spin fluctuations can lead to a net attractive pairing force between electrons with opposite momenta and spin.[42]

Known High-Temperature Superconductors

The discovery of high-temperature superconductivity in YBCO led to the discovery of new copper-oxide superconductors and new superconductor families. The three main families of high-temperature superconductors include cuprates (copper-oxides),[43] nickelates (nickel-oxides),[44] and iron-pnictogens.[45] Hydride superconductors also exist but only operate at high pressures.[46] Cuprates exhibit anisotropies due to a complex perovskite structure. Layered crystal structures feature square planar configurations of transition metal atoms coordinated by anions

(CuO_2, FeAs, NiO planes), separated by planes of other oxides and rare earth metals. The transition metal-anion planes are understood to form the conducting layers where superconductivity emerges.

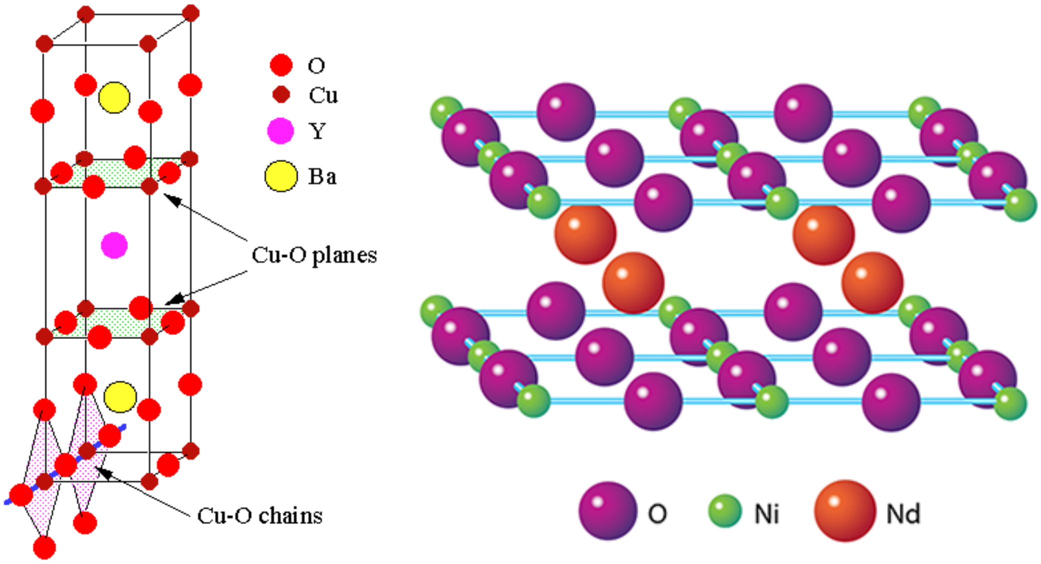

Figure 2-4. *Crystal structure for YBCO pictured left. Infinite layer structure for* $NdNiO_2$ *pictured right.*

In nickelates, superconductivity occurs in infinite layered NiO_2 compounds. Synthetic superlattices created by pulsed laser deposition, such as La_2NiMO_6, are constructed with alternating planes of NiO_2 and MO_2, where M = Al, Ga, Ti. Artificial structures such as La_2NiMO_6 use MO_6 to suppress c-axis electron hopping, enforce the square planar coordination of NiO_2, and mimic cuprates' two-dimensional electron transport mechanism. The T_c of nickelates is far lower than that of cuprates and requires pressure to stabilize.

Iron-based superconductors are either iron-pnictide or iron-chalcogenide compounds (FePn/Ch) and exhibit tetragonal geometry. Iron is not found in a square planar lattice, and appears to activate superconductivity differently, and at lower temperatures, than cuprates and nickelates. High-pressure hydrides, while capable of superconducting at high temperatures, require extreme pressures—often exceeding 150 GPa—which approach those found in the Earth's core (approximately 360 GPa), making practical applications unfeasible.

The most well-known high-temperature cuprate superconductor is $YBa_2Cu_3O_{7-\delta}$ (YBCO), which becomes superconducting at $T_c = 93$ K. Superconducting compounds similar to YBCO, such as $La_{2-x}Sr_xCuO_4$, $Bi_2Sr_2Ca_{n-1}Cu_nO_{2n+4+\delta}$, $Hg_2Sr_2Ca_{n-1}Cu_nO_{2n+2+\delta}$, $Tl_2Sr_2Ca_{n-1}Cu_nO_{2n+3+\delta}$. The quantity noted as δ determines the oxygen content of the sample. Specifically tuning this value determines whether superconductivity will occur and correlates strongly with the critical temperature of the sample. The quantity written as *n* ranges for 1 to 3 and is the number of CuO_2 planes present in the unit cell of these crystals. The number of CuO_2 planes increases the critical temperature of the sample in the bismuth, thallium, and mercury based cuprates. The La-cuprate is called La-214. The names are based on *n*. For instance, when *n* = 3, we have the compounds Bi-2223, Tl-2223, and Hg-1223. These three compounds are cuprates with the highest-known T_c values, at 108 K, 125 K, and 134 K respectively.

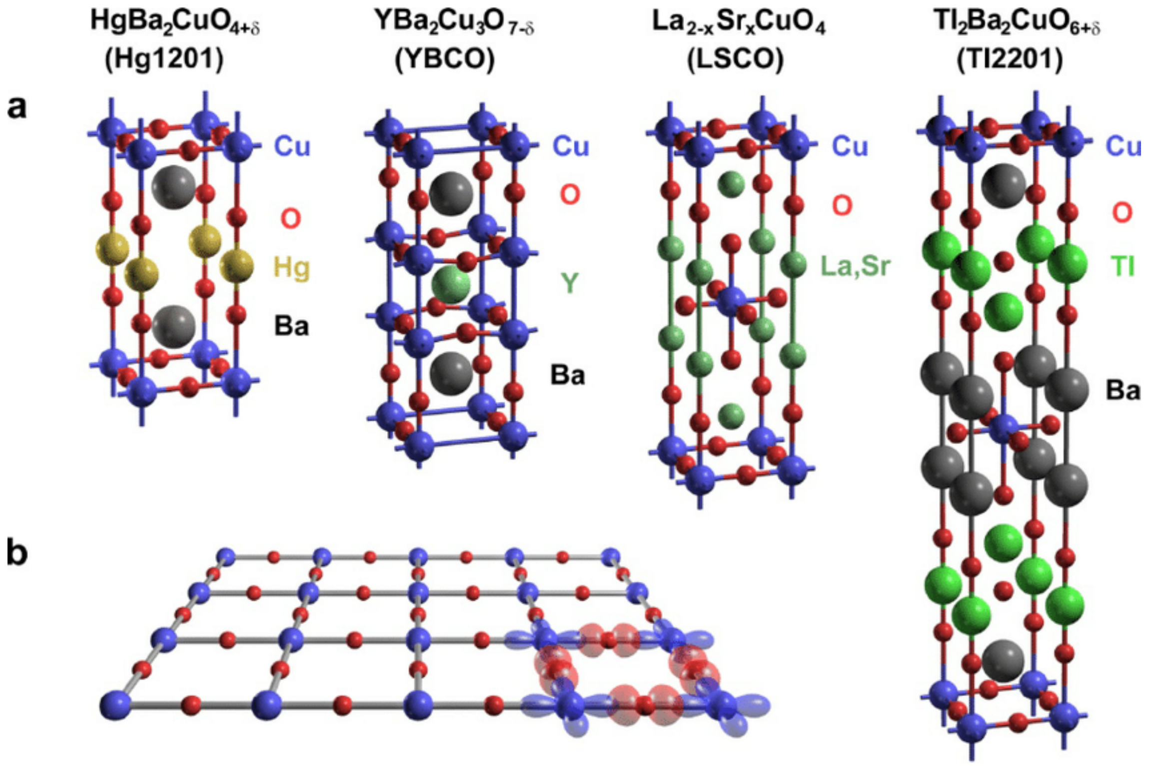

Figure 2-5. *(a) Layered perovskite crystal structures of four known high-temperature cuprate superconductors. These include Hg1201, YBCO, LSCO, and Tl2201. (b) Visualization of the copper-oxide planes in cuprate lattices, with orbital overlap between the Cu^{2+} $d_{x^2-y^2}$ orbitals and O^{2-} p_x and p_y orbitals.*[47]

After the discovery of the high-temperature copper oxide superconductors in the 1980s, superconductor discovery has slowed. Despite the emergence of other related families, such as the nickelates and iron-based superconductors, the exploration of cuprates has slowed.

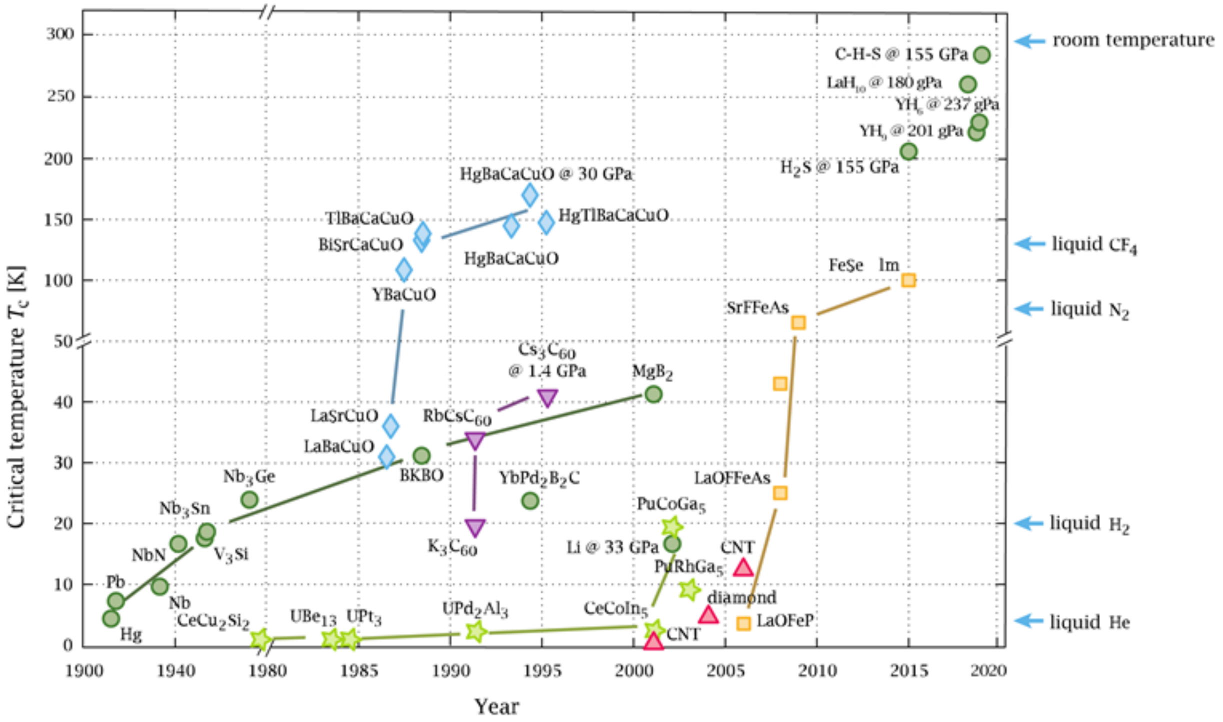

Figure 2-6. *Chart showing the discovery of superconductors over time. The era of high-temperature copper oxides (blue) ended by the 2000s. Iron-based superconductors (yellow) are more recent, but with lower critical temperatures. The hydrides (green) are the most recent but only activate under high-pressures.*[48]

Structural & Geometric Analysis

Layered Perovskite Structure and Jahn-Teller Distortion

HTS cuprates and nickelates share a common layered structure of transition-metal-oxide planes (MO_2, for M = Cu, Ni) separated by insulating cation or oxide planes. The copper oxide structure is a unit cell resembling a perovskite. Nickelates adopt an infinite-layer structure closely analogous to a cuprate with the apical oxygens removed. Due to the octahedral coordination and d^9 electron configuration of the Cu^{2+} ions in the layered perovskite structures, the CuO_6 octahedra experience an elongation of the apical oxygens known as Jahn-Teller distortion. Jahn-Teller distortion drives a splitting of the degeneracy in the e_g* antibonding orbital, where the d_{z^2} orbitals of the elongated axial ligands are higher in energy than the planar $d_{x^2-y^2}$ and d_{xy}, d_{xz}, d_{yz} orbitals. The parent compound, $LaCu_2O_4$, of the first discovered high-temperature superconductor, $La_{2-x}(Sr,Ba)_xCu_2O_4$ (LSCO), displays elongation on the c-axis of the CuO_6 octahedron.

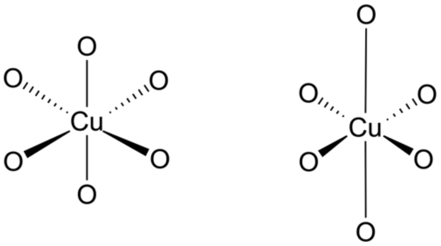

Figure 2-7. Jahn-Teller distortion in CuO_6 octahedron. An ideal, undistorted octahedron is pictured left. Jahn-Teller distortion, specifically the elongation of the vertical axis, is pictured right.

CuO_6 Octahedron: Planar Geometry and Apical Oxygens

The planar atoms of the CuO_6 octahedron form the CuO_2 planes that are central to superconductivity in high-temperature cuprates. CuO_2 planes act as charge-carrying layers, verified by anisotropic resistivity measurements: in-plane resistivity is orders of magnitude lower than out-of-plane resistivity. As established by Jahn-Teller distortion of the octahedron, the in-plane Cu-O bonds of LSCO (1.90-1.93 Å) are shorter than the apical Cu-O bonds (2.40-2.47 Å). This trend in bond length is also seen in YBCO (1.96 Å < 2.34 Å), Bi-2212 (with apical oxygen bonds ranging from 2.2 to 2.6 Å), and others. This contraction of the planar bond lengths compared to the elongation of the apical bond lengths reflects the lifting of degeneracy of the e_g orbitals, lowering the energy of the $d_{x^2-y^2}$ orbital, which is primarily involved in conduction within the CuO_2 plane.[49,50]

In an ideal layered perovskite structure, the CuO_2 planes form 180˚ Cu-O-Cu bond angles. Structural phase transitions (specifically from tetragonal to orthorhombic phases) occur at lower temperatures, introducing octahedral tilts that reduce the planar angle. In low-temperature orthorhombic LSCO, the Cu–O–Cu angle reduces to approximately 174°, while in YBCO it is close to 176–178° depending on oxygen content and temperature. These buckling distortions displace in-plane oxygens out of the CuO_2 plane, which can disrupt the coherent overlap of Cu 3d and O 2p orbitals, reducing pairing strength between Cooper pairs and thus decreasing T_c.

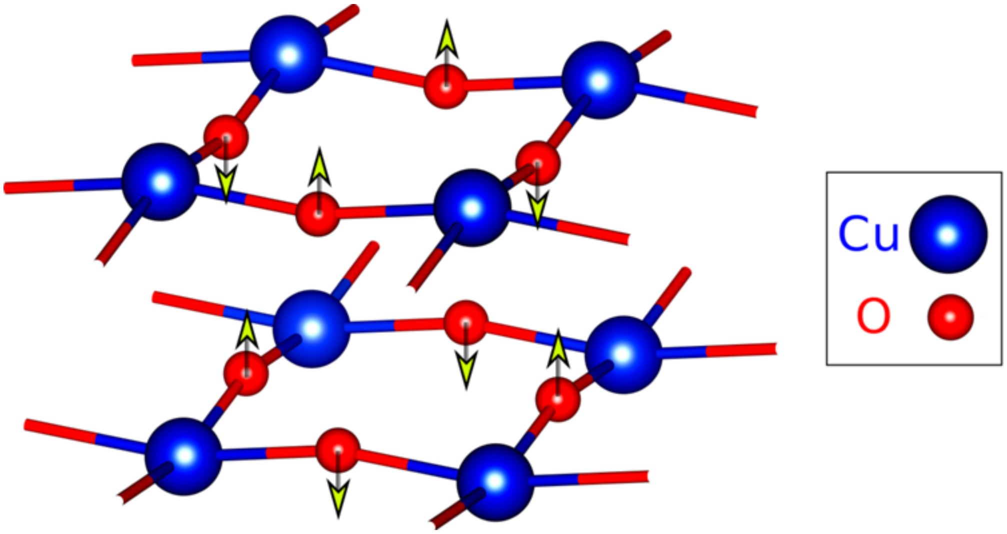

Figure 2-8. *Buckling of the CuO2 planes in YBCO with the antiferromagnetic, alternating up-down spins shown.*[51]

HTS cuprates such as Bi-2212, Tl-2201, Hg-1201 exhibit little to know buckling.[52, 53] The Cu-O-Cu angle remains nearly 180˚ and the CuO_2 planes remain flat. These superconducting compounds also exhibit higher critical temperature, supporting the trend that a planar geometry that maximizes Cu-O-Cu orbital overlap enhances the strength of Cooper pairing.

Apical oxygens influence the spacing between layers and therefore also influence superconductivity. The distance between the Cu and the apical O affects the energy splitting between the $d_{x^2-y^2}$ and d_{z^2} orbitals found in Jahn-Teller distorted compounds. In Tl-2201 and Hg-1201, the apical O is closer to Cu (~1.86–2.2 Å), creating a compressed CuO_6 geometry.

Compression of the CuO_6 octahedron raises the energy of the d_{z^2} orbital relative to the $d_{x^2-y^2}$ orbital. Studies have observed a correlation between shorter Cu-O apical distances and higher T_c.

The number of CuO_2 planes in the unit cell also correlates with enhanced superconductivity. In the bismuth cuprates, where n is the number of CuO_2 planes: Bi-2201 (n=1), Bi-2212 (n=2), and Bi-2223 (n=3) correlates with $T_c \approx 30$ K, 90 K, and 110 K respectively.[52] Increasing the number of CuO_2 planes per unit cell correlates with an increasing T_c, suggesting that interlayer coupling or other effects due to the proximity of adjacent CuO_2 planes enhances the stability of the superconducting state.

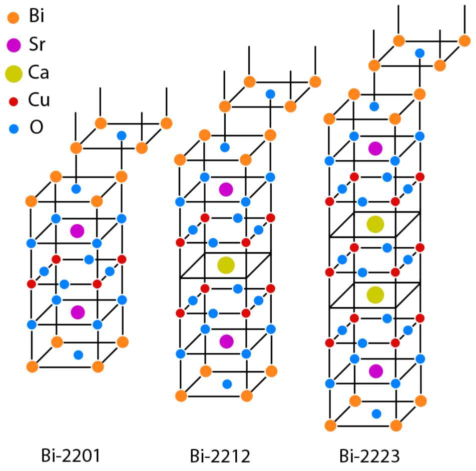

Figure 2-9. *Bismuth superconductors for different numbers of CuO_2 planes (n = 1, 2, 3).*[54]

Lattice Symmetry and Octahedral Tilts

Lattice symmetry governs the electronic structure, spin interactions, and superconducting behavior of HTS compounds. Tilting of the CuO_6 octahedra as a result of deformation directly influences bond angles, lattice parameters, and orbital overlap with the CuO_2 planes.

In an ideal layered perovskite, the CuO_6 are undistorted, and the crystal exhibits tetragonal symmetry (space group I4/mmm) with the Cu-O-Cu bond angles at 180°. This configuration maximizes orbital overlap between the Cu $3d_{x^2-y^2}$ and O $2p_x/2p_y$ orbitals, enhances magnetic superexchange between spins, and is essential for superconductivity. The parent compounds of cuprates at low doping levels or low temperatures deviate from this ideal planar geometry due to octahedral tilts. These tilts are often thermally activated or doping-dependent, causing the symmetry of the lattice to decrease from tetragonal to orthorhombic.

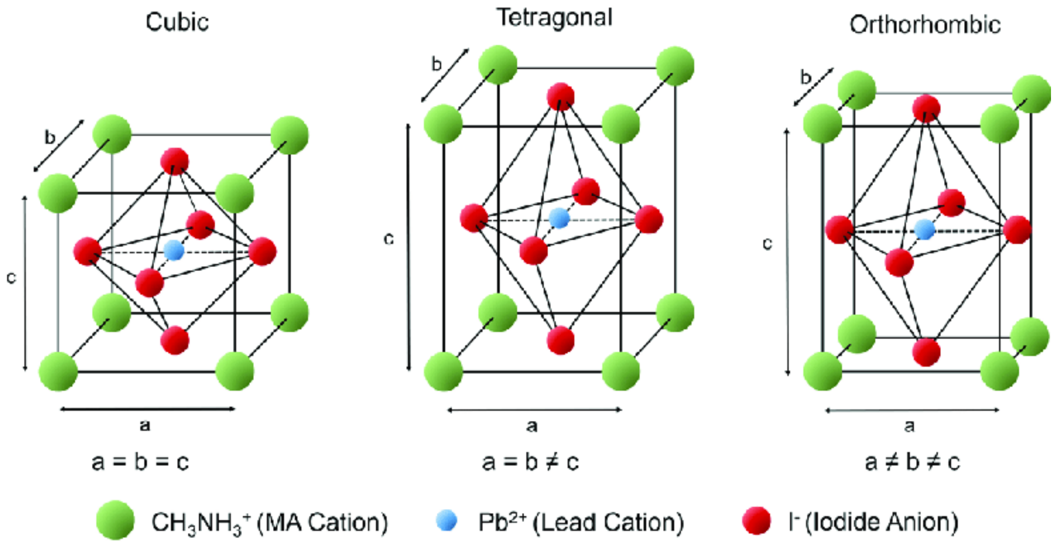

Figure 2-10. Cubic, tetragonal, and orthorhombic crystal structures for the same solid state structure. Temperature conditions effects the phase of the lattice.[55]

Charge Reservoir Layers

The CuO_2 planes in HTS cuprates are separated by charge reservoir layers serving dual function: first, the geometry stabilizes the lattice structure; second, these layers control the charge carrier concentration in the CuO_2 planes. In LSCO, the reservoir layer consists of a cubic (La,Sr)2O2 block. Doping La^{3+} sites with Sr^{2+} introduces holes into the CuO_2 plane, requiring the Cu ions to oxidize from Cu^{2+} to Cu^{3+} to balance the charges. This alters the average oxidation state of copper throughout the lattice.

In YBCO, the charge reservoir function is fulfilled by a Cu-O chain layer. A-site cations (Y^{3+}, Ba^{2+}) stabilize the structure. The Cu-O chain acts as both a structural spacer and a dynamic charge reservoir. When YBCO is fully oxygenated ($\delta \approx 0$), this layer forms one-dimensional CuO chains with copper ions in the chain having an oxidation state close to Cu^{1+}; the CuO_2 planes have copper ions with an oxidation state close to Cu^{2+}. As δ increases and oxygen Is removed from the chains, T_c decrease, with superconductivity not present at the limit of $\delta = 1$.

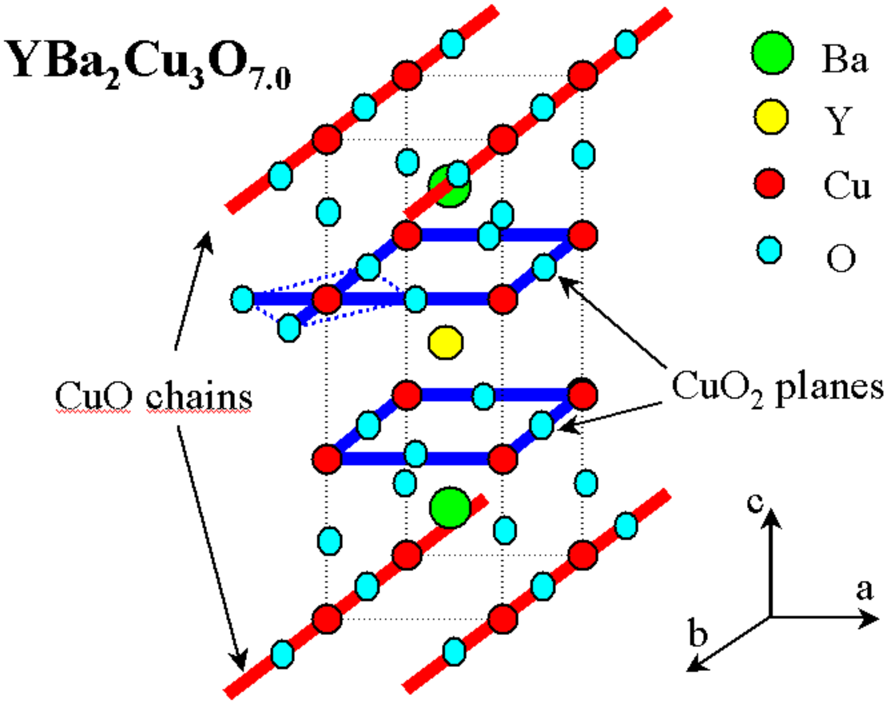

Figure 2-11. *CuO charge reservoir chains and CuO2 charge carrier planes in an ideal YBCO lattice.*[56]

In Bi-, Tl-, and Hg-based cuprates, the reservoir layers are composed of heavy metals (Bi^{3+}, Tl^{3+}, Hg^{2+}) coordinated with oxygen, forming BiO, TlO, or HgO layers that sit between the CuO_2 blocks. Bi-2212 follows a stacking sequence of: BiO-SrO- CuO_2-Ca-CuO_2-SrO-BiO, where BiO layers behave as the principal charge reservoirs. Similar to the CuO chains of YBCO, the oxygen content of the lattice directly impacts the number of O atoms found in the BiO layers.

In the Hg-cuprates, such as Hg-1201,[57] the HgO layer sits between BaO and CuO_2. Unlike YBCO, where oxygen atoms are incorporated into chains, excess oxygen in Hg-1201 occupies interstitial sites near the Hg plane. The location of these oxygen atoms is at the apical oxygen site, and has the shortest distance of all cuprates between the apical O and the nearest Cu site. This compressed apical geometry elongates the planes by an inverse Jahn-Teller distortion, and may contribute to the high- T_c of Hg-1223 at 134 K (-139˚C, -218˚F), the highest recorded T_c of a superconductor at ambient pressures.

Doping Effects on Structure

Doping controls the electronic carrier concentration present in the CuO_2 planes and induces significant structural modifications throughout the crystal lattice that determine whether or not a given structure can enter the superconducting state. All known cuprate superconductors are derived from Mott insulating parent compounds, a class of antiferromagnetic materials are expected to condct electricity according to conventional band theory, but turn out to be insulators at low temperatures. In these Mott insulators, Cu exists as Cu(II) with a $3d^9$ electronic configuration, resulting in strong electron correlations and localized magnetic moments. Doping alters the formal oxidation state of copper by either introducing holes ($Cu^{2+} \rightarrow Cu^{3+}$) or electrons (reducing $Cu^{2+} \rightarrow Cu^{1+}$) depending on the dopant species and its site. Site substitution (for instance, switching La^{3+} with Sr^{2+}) and controlling the oxygen content (δ) is how this is modified experimentally.

In YBCO, doping is achieved by varying the oxygen content, δ. Adding oxygen to the Cu–O chain layer (i.e., decreasing δ toward 0) increases the hole concentration in the CuO_2 planes and induces a phase change from tetragonal to orthorhombic, which occurs around $\delta \approx 0.6–0.7$. At high δ (~0.9–1.0), when most chain oxygen is removed, the structure becomes tetragonal and non-superconducting. In Bi- and Hg-based cuprates, doping is controlled via excess oxygen in the BiO or HgO layers, which correlates with increasing T_c.

For nickelate structures without charge resevoir layers or apical oxygens for doping via controlling the oxygen content, doping relies entirely on cation site substitution. The nickelate structure, such as that found in $Nd_{1-x}Sr_xNiO_2$, remains in the tetragonal state down to low temperatures.

Electronic Properties Analysis

The electronic structure of high-T_c superconductors is strongly influenced by their geometry, exhibiting recurring features that may be central to an unknown, unconventional pairing mechanisms. The lattice geometry, which determines the shape of orbital overlaps and electron band dispersion. A high electron density of states is also reported near the Fermi level, displaying critical points such as Van Hove singularities (*Figure 2-12*). These features may promote instabilities that favor a specific pairing mechanism.

Orbital Character and Band Dispersion

CuO_2 planes are the primary carriers of electronic transport and Cooper pairing in superconductors, and this is a result of the orbital characteristics of the structure. In the undoped parent compounds of HTS cuprates, such as La_2CuO_4 and $YBa_2Cu_3O_6$ (δ=1), Cu exists in the $3d^9$ configuration as Cu(II). This configuration includes one electron hole (the d-orbital shell fills at d^{10} electrons). Jahn-Teller distortion lifts the degeneracy of the e_g^* antibonding orbital, placing the $3d_{x^2-y^2}$ orbital lying highest in energy. This orbital overlaps strongly with in-plane oxygen $2p_x$ and $2p_y$ orbitals, results in an antibonding, conduction band near the Fermi level with one electron per Cu site when undoped. This results in a narrow conduction band.

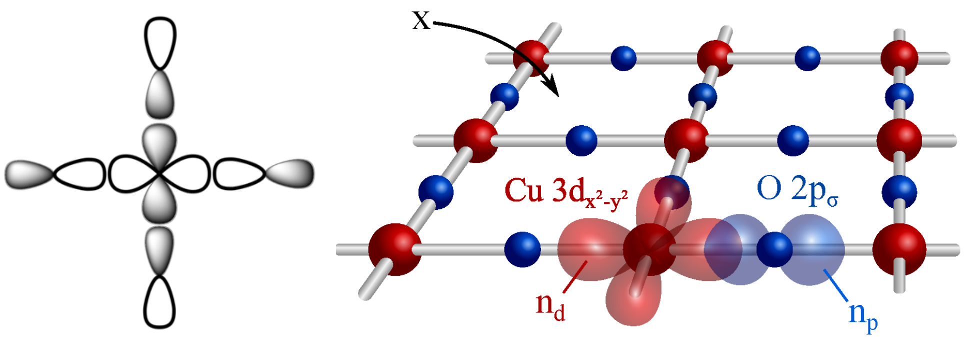

Figure 2-12. Left: Diagram showing orbital bonding between the central $d_{x^2-y^2}$ *orbital and the four exterior* p_x *and* p_y *orbitals. Right: The same orbitals in a repeating square planar* CuO_2 *lattice.*

The density of states (DOS) near the energy levels relevant for superconductivity in cuprate materials is primarily shaped by the CuO_2 planes, which govern their low-energy electronic behavior. In their undoped form—such as in La_2CuO_4 or $YBa_2Cu_3O_6$—these materials act as antiferromagnetic Mott insulators, where strong electron-electron repulsion prevents conduction.

To probe these electronic properties, researchers use Angle-Resolved Photoemission Spectroscopy (ARPES), a powerful experimental technique that measures how electrons behave inside a material. ARPES works by shining light onto a sample to eject electrons, then measuring the energy and angle of those electrons as they leave. From this, one can reconstruct how tightly electrons are bound in the material and how they respond to excitations. In cuprates, ARPES reveals that the electronic structure is highly two-dimensional, confined largely to the CuO_2 planes, and shows clear energy dispersion, meaning that the energy of electrons changes smoothly with their quantum state.[58]

Upon doping the system (adding carriers), ARPES detects a transfer of spectral weight from incoherent, high-energy electronic states—associated with the insulating Mott phase—to coherent, low-energy quasiparticle states, which are indicative of metallic or superconducting behavior. This transition supports the idea that strong electron correlations dominate the physics of cuprates, as the electrons do not behave like simple non-interacting particles. Instead, the system gradually evolves from an insulator to a superconductor through the emergence of collective, low-energy excitations that ARPES can directly observe.[59]

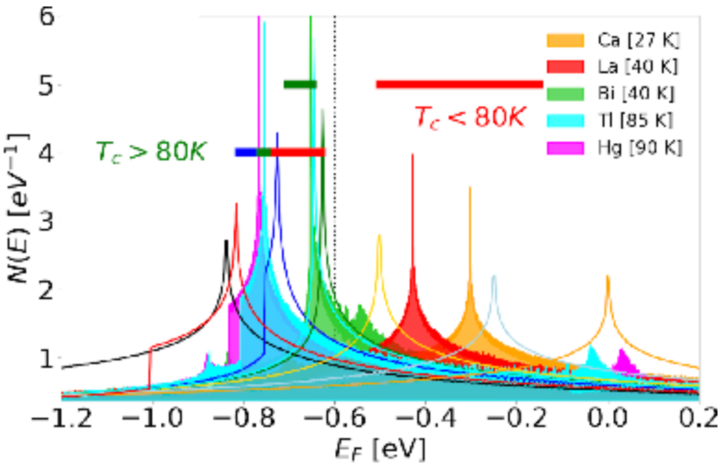

Figure 2-13. *The characteristic Van Hove singularities found near the Fermi level (E_F) in the electron density of states of different high-T_c cuprates.*[59]

Jahn Teller distortion controls the height of apical oxygens, influence the crystal field splitting between the Cu $d_{x^2-y^2}$ and O d_{z^2} orbitals. Shorter apical Cu-O distances raise the d_{z^2} level, enhancing $d_{x^2-y^2}$ dominance near the Fermi level.[60]

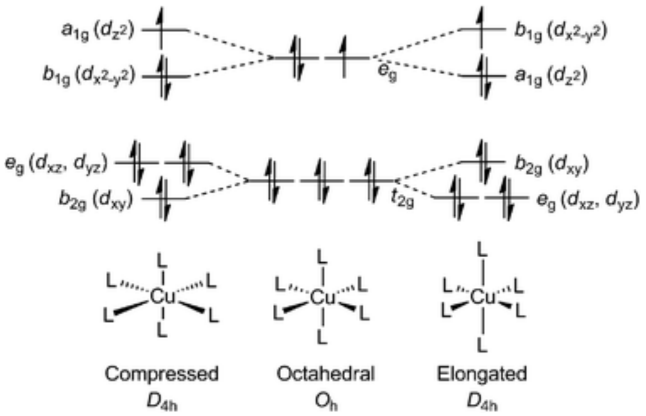

Figure 2-14. *Jahn-Teller distortion degeneracy lifting for compressed, elongated and standard octahedral metal-ligand complexes.*

Chapter 3 – Machine Learning

Neural Networks

Artificial neural networks (ANNs) are a class of machine learning models inspired by the structure of biological neural systems. ANNs are composed of interconnected layers of simple processing units called neurons, which collectively learn to approximate functions from data by linear regression. ANNs are capable of modeling complex, non-linear, high-dimensional data.

A basic feedforward neural network consists of an input layer, hidden layers, and an output layer. Input layers receive a feature vector x. Each hidden layer includes neurons where the weights of the input feature are computed and passed through an activation function, sigma:

$$h_i^{(l)} = \sigma\left(\sum_j w_{ij}^{(l)} h_j^{(l-1)} + b_i^{(l)}\right)$$

Where $w_{ij}^{(l)}$ are the weights from neuron j in the previous layer, $b_i^{(l)}$ is a linear bias, and σ is a non-lienar activation function, such as ReLU or tanh (Figure 3-1), which introduces non-linearity into the model, which enables the network to approximate complex mapping between input and output data. The final layer, called the output layer, takes the transformed representation from previous layers and maps it to a prediction or decision, reflecting what the model learned during training.

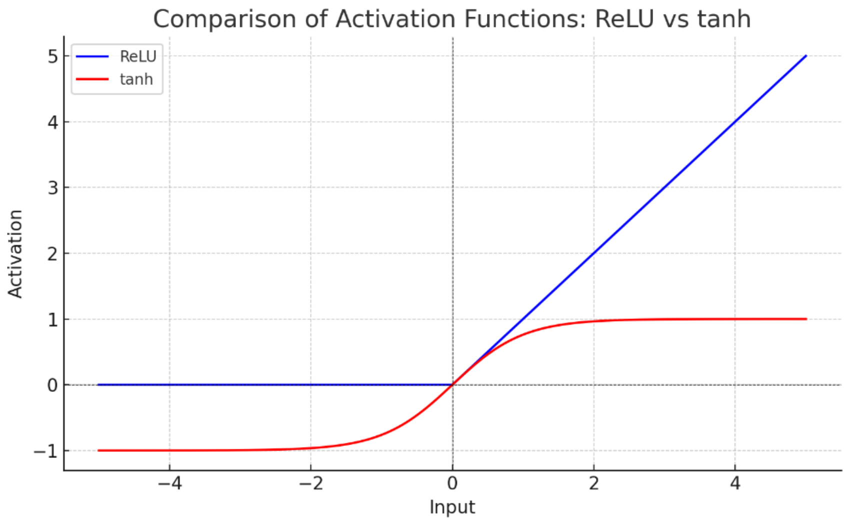

__Figure 3-1__. Rectified Linear Unit (ReLU) and tanh(x) activaton functions plotted. Activation functions non-linearize the learned parameters of the model.

Training a Neural Network

The network learns by minimizing a loss function over a dataset of input-output pairs (x, y). For regression tasks, a common choice of loss function is the mean squared error (MSE):

$$\text{MSE} = \frac{1}{n}\sum_{i=1}^{n}(y_i - \hat{y}_i)^2$$

The parameters (or weights, $w_{ij}^{(l)}$) in a neural network are updated during training using optimization methods like Stochastic Gradient Descent (SGD) or Adam. These algorithms aim to minimize the loss function, which measures how far the model's predictions are from the actual targets. To do this, the model uses a process called backpropagation. Backpropagation works by calculating how much each weight in the network contributes to the overall error (loss). It then computes the gradient—a measure of how the loss changes with respect to each weight—and adjusts the weights in the direction that reduces the loss. This is repeated across many iterations until the model learns to make accurate predictions.

Graph Neural Networks

Traditional neural networks are not well-suited for irregular or structured data—like molecules, crystals, or any system where the relationships between elements matter more than their position in a fixed grid. Graph Neural Networks (GNNs) are a powerful extension of neural networks designed to handle this kind of relational or spatially structured data. To understand this, we turn to graph theory, a field of mathematics that studies graphs—structures made up of nodes (which represent entities like atoms) and edges (which represent connections or interactions, like chemical bonds).

A graph, G, is defined as:

$$G = (V, E)$$

Where V is the set of nodes corresponding to atoms and E is a set of edges representing atomic interactions (i.e., bonds). Each node $v_i \in V$ is associated with a feature vector $\boldsymbol{h}_i$ that includes encoded information such as the atomic number and electronegativity. Edges $(i, j) \in \mathrm{E}$ encodes information such as the interatomic distance.

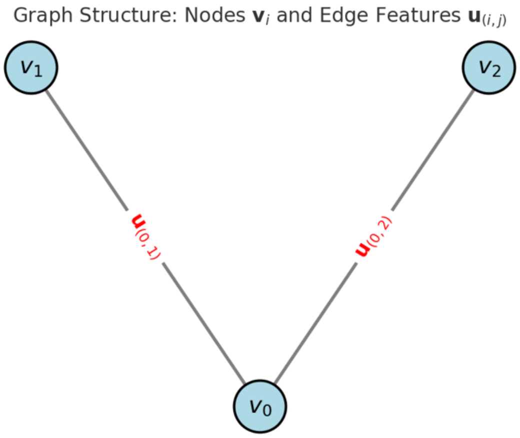

Figure 3-2: Simple graph structure for node v_0, neighbor nodes v_1 and v_2, and the edges $u_{(0,1)}$ and $u_{(0,2)}$ between them.

GNNs learn by iteratively updating node features through a convolution algorithm. At each layer t, the feature of node v_i is updated based on its neighbors:

$$v_i^{(t+1)} = Conv\left(v_i^{(t)}, v_j^{(t)}, u_{(i,j)k}\right), (i,j)_k \in G$$

Where $v_i^{(t)}$ is the node feature vector of atom i at layer t, $v_j^{(t)}$ is the node feature vector of the neighboring j atom at layer t, and $u_{(i,j)k}$ is a feature vector for edges $(i,j)_k$. After several passes in the convolution layers, a pooling operation aggregates node features into a single vector representing the crystal:

$$v_G = POOL\left(\left\{v_i^{(T)}: i \in V\right\}\right)$$

Where $v_i^{(T)}$ is the node feature vector after a total of $t_1, t_2, \ldots, T$ convolution steps.

Crystal Graph Convolutional Neural Network

Following this process for crystal structures is the crystal graph convolutional neural network (CGCNN) algorithm, an algorithm that formed the basis of materials property predictions. The specific input to a CGCNN consists of crystallographic information files (CIFs) that encode information, such as the coordinates, atom types, lattice vectors, and space group symmetry on the unit cell of a given crystal.

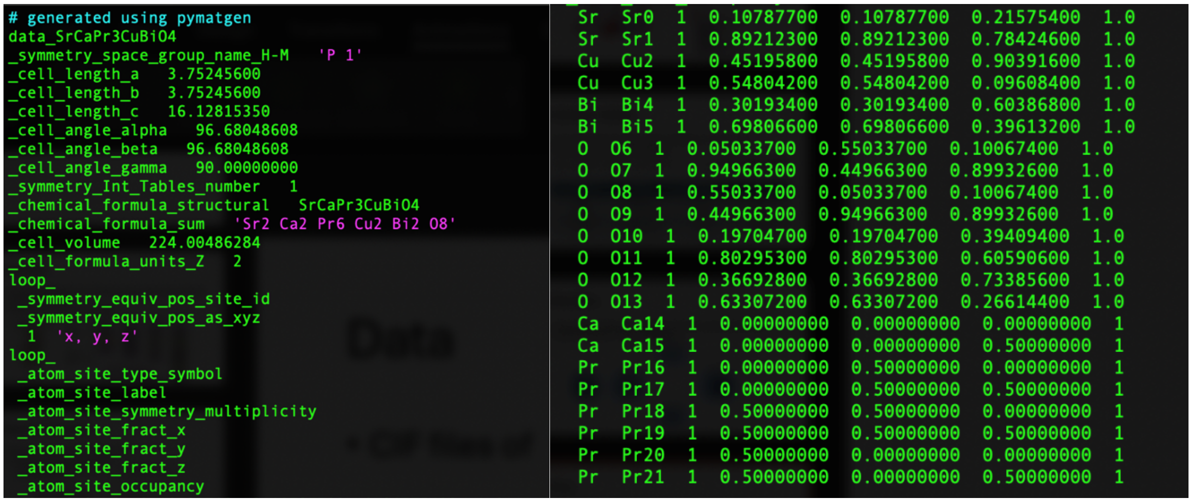

```
# generated using pymatgen
data_SrCaPr3CuBiO4
_symmetry_space_group_name_H-M   'P 1'
_cell_length_a   3.75245600
_cell_length_b   3.75245600
_cell_length_c   16.12815350
_cell_angle_alpha   96.68048608
_cell_angle_beta   96.68048608
_cell_angle_gamma   90.00000000
_symmetry_Int_Tables_number   1
_chemical_formula_structural   SrCaPr3CuBiO4
_chemical_formula_sum   'Sr2 Ca2 Pr6 Cu2 Bi2 O8'
_cell_volume   224.00486284
_cell_formula_units_Z   2
loop_
 _symmetry_equiv_pos_site_id
 _symmetry_equiv_pos_as_xyz
  1  'x, y, z'
loop_
 _atom_site_type_symbol
 _atom_site_label
 _atom_site_symmetry_multiplicity
 _atom_site_fract_x
 _atom_site_fract_y
 _atom_site_fract_z
 _atom_site_occupancy
```

```
  Sr  Sr0  1  0.10787700  0.10787700  0.21575400  1.0
  Sr  Sr1  1  0.89212300  0.89212300  0.78424600  1.0
  Cu  Cu2  1  0.45195800  0.45195800  0.90391600  1.0
  Cu  Cu3  1  0.54804200  0.54804200  0.09608400  1.0
  Bi  Bi4  1  0.30193400  0.30193400  0.60386800  1.0
  Bi  Bi5  1  0.69806600  0.69806600  0.39613200  1.0
  O  O6  1  0.05033700  0.55033700  0.10067400  1.0
  O  O7  1  0.94966300  0.44966300  0.89932600  1.0
  O  O8  1  0.55033700  0.05033700  0.10067400  1.0
  O  O9  1  0.44966300  0.94966300  0.89932600  1.0
  O  O10  1  0.19704700  0.19704700  0.39409400  1.0
  O  O11  1  0.80295300  0.80295300  0.60590600  1.0
  O  O12  1  0.36692800  0.36692800  0.73385600  1.0
  O  O13  1  0.63307200  0.63307200  0.26614400  1.0
  Ca  Ca14  1  0.00000000  0.00000000  0.00000000  1
  Ca  Ca15  1  0.00000000  0.00000000  0.50000000  1
  Pr  Pr16  1  0.00000000  0.50000000  0.00000000  1
  Pr  Pr17  1  0.00000000  0.50000000  0.50000000  1
  Pr  Pr18  1  0.50000000  0.50000000  0.00000000  1
  Pr  Pr19  1  0.50000000  0.50000000  0.50000000  1
  Pr  Pr20  1  0.50000000  0.00000000  0.00000000  1
  Pr  Pr21  1  0.50000000  0.00000000  0.50000000  1
```

Figure 3-3. *Example CIF file for a bismuth-based cuprate superconductor.*

The elements of the periodic table are represented numerically by a method known as one-hot encoding, which represents categorical variables as binary vectors of a fixed length, N. Information such as electronegativity, atomic radius, and atomic mass are discretized into histogram-like bins. Concatenating these histograms creates a composite feature vector for each atom.

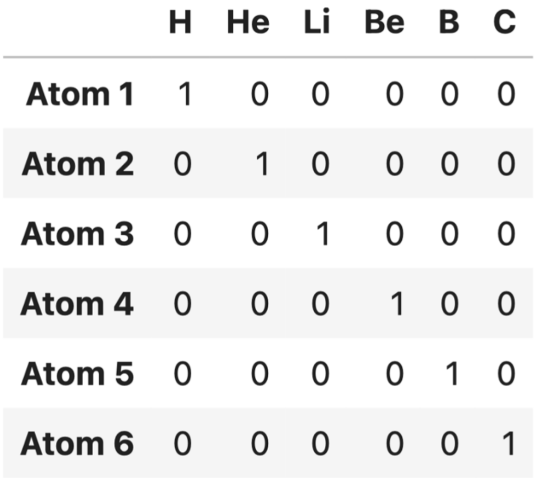

	H	He	Li	Be	B	C
Atom 1	1	0	0	0	0	0
Atom 2	0	1	0	0	0	0
Atom 3	0	0	1	0	0	0
Atom 4	0	0	0	1	0	0
Atom 5	0	0	0	0	1	0
Atom 6	0	0	0	0	0	1

Figure 3-4. *Simplified one-hot encoding example for the first six elements of the periodic table, showing only categorization by atomic number. Other vectors representing other atomic properties (electronegativity, atomic radius, etc.) are concatenated to create binary descriptors of each element.*

Node and edge feature vectors are built from these CIF files. The node feature vector, a representation of the crystal atom types, are mapped to their respective one-hot encoded vectors.

The edge feature vectors represent atom pairs between the 12 nearest neighbors within a cutoff radius (default 8 Å), capturing the relationships between local chemical environments. The interatomic distance between atoms *i* and *j* is computed using the Euclidean norm:

$$d_{ij} = |r_i - r_j|_2 = \sqrt{\left(x_i - x_j\right)^2 + \left(y_i - y_j\right)^2 + \left(z_i - z_j\right)^2}$$

The Gaussian basis expansion is applied to encode this scalar distance into a smooth, differentiable vector:

$$\phi_k\left(d_{ij}\right) = \exp\left(-\frac{\left(d_{ij} - \mu_k\right)^2}{\sigma^2}\right)$$

Where μ_k is the Gaussian mean and σ is the Gaussian width.

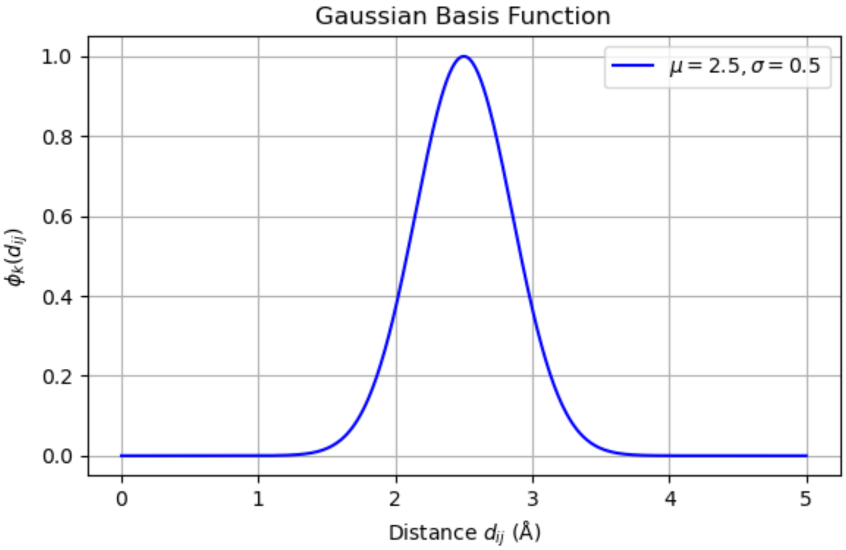

Figure 3-5. *Gaussian basis function, a normal distribution, visualized with mean = 2.5 and standard deviation = 0.5.*

CDVAE: Generative AI

Generative AI has seen an explosion in use with the rise of commercially successful algorithms such as OpenAI's ChatGPT, Google's Gemini, and the open-source Chinese-developed DeepSeek. The Crystal Diffusion Variational Autoencoder (CDVAE) is a generative

AI model developed for the purpose of learning the underlying probability distribution of crystal structures to enable the generation of novel, chemically stable crystal candidates. CDVAE relies on graph representations of crystals and uses a graph neural network architecture to map input structures to output properties as seen in the CGCNN. CDVAE uses a variational autoencoder to probabilistically generate new structures.[61]

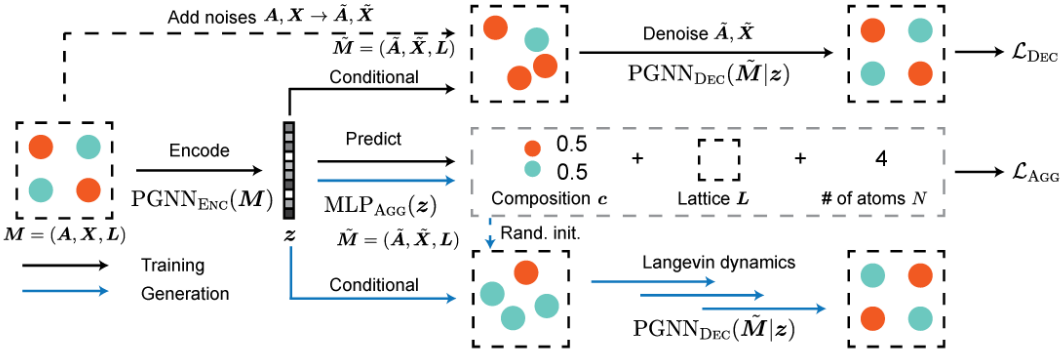

Figure 3-6. *Architecture of the CDVAE algorithm.*[61]

Variational Autoencoders

A Variational Autoencoder (VAE) is a type of neural network that learns how to generate new data by first understanding the patterns in a training dataset. It’s especially useful for creating variations of images, molecules, or crystal structures. The VAE has two main components: an encoder, which compresses the input data into a compact, abstract representation called the latent space, z. And a decoder, which tries to rebuild the original data from this compressed form.

The VAE maps the data to a probability distribution defined by a mean and standard deviation. This lets the model sample different points within that distribution, capturing natural variations in the data. During training, the VAE learns two things at once: how to reconstruct the input data from a sample in the latent space, and how to keep the latent space smooth and organized by shaping it to follow a normal distribution. This structure allows VAEs to generate entirely new, yet stable examples—not by memorizing the data, but by learning the underlying structure and variability.

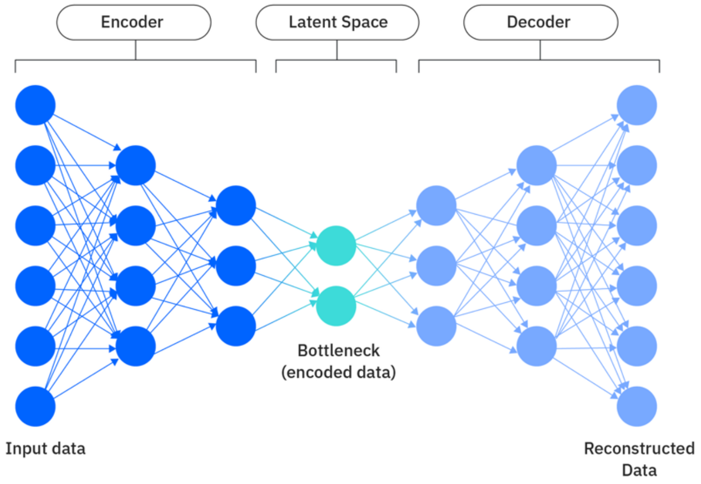

Figure 3-7. *Source: IBM. General architecture for variational autoencoder.*

In CDVAE, this concept is applied to crystal structures: the model encodes crystal graphs into a latent space, then decodes samples from that space to generate new, plausible crystal structures, guided by physical and chemical constraints. During training, a periodic graph neural network (PGNN) encoder embeds input crystal structures—described by atom types, fractional coordinates, and lattice vectors— into a latent space. A decoder, also built on a SE(3)-equivariant PGNN architecture,[62] performs conditional score matching to denoise randomly initialized structures into chemically plausible materials.

A key feature of CDVAE is its incorporation of annealed Langevin dynamics[63] to iteratively refine atom positions and types based on learned gradients, effectively simulating a descent toward lower-energy configurations. This process approximates the behavior of atoms in a harmonic force field, where the network learns to model the forces restoring atoms to equilibrium positions.

These enhancements enable CDVAE to not only reconstruct known materials but also generate novel candidates that exhibit realistic properties and structural diversity. Empirical evaluation demonstrates superior performance across tasks such as structure reconstruction and property optimization compared to prior generative models.

Chapter 4 – Workflow

A closed-loop, AI-assisted workflow was developed to accelerate the discovery of new high-temperature superconductors. The process begins with a curated dataset of known inorganic materials, represented by crystallographic information files (CIFs), which serve as training input for a generative machine learning model (CDVAE). This model learns the underlying structural and compositional patterns of stable compounds and outputs novel crystal candidates consistent with these trends. CDVAE is trained via a graph neural network to learn the relationship between input superconducting compounds and their corresponding critical temperatures. The generated structures are relaxed using low-cost computational methods to resolve stable configurations.[64, 65] Subsequently, the relaxed candidates are evaluated by a fast property prediction model[66] (ALIGNN) to estimate thermodynamic stability and alignment with target features, such as band gap.

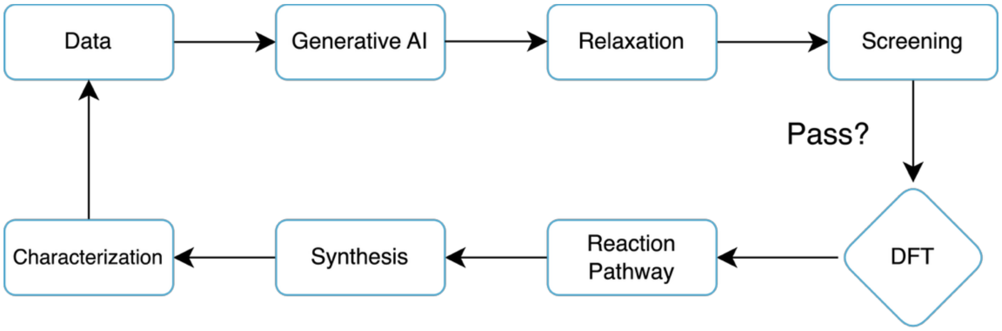

Figure 4-1. Proposed workflow for an AI-accelerated closed loop workflow for discovering new high-temperature superconductors.

First-principles calculations, such as density functional theory (DFT), are used to validate the electronic structure, total energy, and stability of relaxed candidates. If a candidate is computationally confirmed to be stable—and potentially superconducting—synthesis pathways are devised based on precursors, thermochemical feasibility, and structural similarity to known phases. Upon synthesis of new samples, the final step is to characterize the material for superconducting properties (e.g., critical temperature, resistivity, and magnetic response). Then phase purity and structure are validated via X-ray diffraction (XRD), which remains the most definitive method of structural verification.

Whether the material exhibits superconductivity or not, the experimentally realized structure is incorporated back into the training dataset, enabling iterative retraining of the generative model with progressively more accurate structure–property relationships. This adaptive loop systematically explores unexplored compositional and structural regimes of HTS materials, reducing reliance on heuristic trial-and-error approaches. By learning directly from verified structural and electronic data, the AI model can uncover unknown correlations between these structures. Applying a data-driven pathway to the problem of high-temperature superconductivity may overcome the current theoretical limitations in understanding the physics of the pairing mechanism, the main bottleneck in discovering new HTS compounds.

While the proposed AI-guided workflow offers an iterative approach for discovering high-temperature superconductors, its practical implementation is limited by our experimental constraints. The absence of advanced structural characterization tools prevents definitive verification of the synthesized crystal structures. The feedback loop between synthesis and data retraining remains incomplete, and the workflow relies heavily on indirect indicators of success, such as Meissner effect observations and resistivity measurements. This incomplete validation pathway also relies on manual tuning of model outputs to achieve desired results. Although the generative AI model employed provides guidance for exploring the materials space, lacking high-resolution structural confirmation limits our approach from improving model performance on structural-property relationships. Continued development of this discovery pipeline will therefore require access to precise structural and electronic characterization techniques to fully close the loop and realize the predictive power of the method. The workflow we used was:

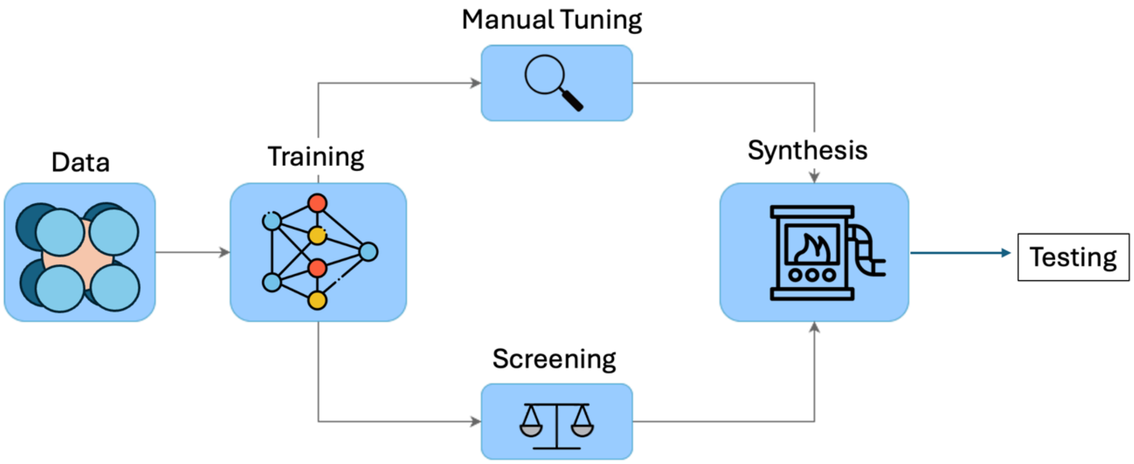

Figure 4-2. *The exact workflow we developed and tested. Limited by the final step of structural characterization, the feedback loop cannot be complete with new, exact structures to retrain the generative AI model.*

Our future work will include employing DFT calculations on new structures to discover their relaxed structures and electronic structure. These results will be compared with XRD characterization of the synthesized sample's true structure.

Using a dataset of known high-temperature superconductors—mostly high-temperature cuprates—a generative AI model was trained to predict new structures based on the relationship between the crystals and their critical temperatures. Structures outputted were mostly unstable, so manual tuning was employed to adjust the stoichiometry of outputs to reflect electrically neutral compounds with a favorable average oxidation state of the Cu atoms. Screening way employed using the ALIGNN model to quickly assess whether candidates were stable. Synthesis relied on the solid-state reaction for creating polycrystalline samples. These samples were then tested for superconductivity with liquid nitrogen, and characterized for magnetism by Gouy's method, and for oxygen content and average copper oxidation state by iodometry.

Tools Used & Developed

A computational workflow was established to automate the design and screening of candidate high-temperature superconducting materials. The Crystal Diffusion Variational Autoencoder (CDVAE), a generative model for crystal structures, was employed for two tasks: (1) generating outputs that reflect the input data and (2) generating outputs optimized for a trained property. In this case, that property was the superconducting critical temperature, T_c.

The first trial trained CDVAE on cuprate CIF files from the 3DSC dataset. Nearly all of these files were doped, thus including fractional sites in the unit cell. Using Materials Project API, each doped unit cell was approximated to its parent unit cell, decreasing the size of the data below 100 datapoints.

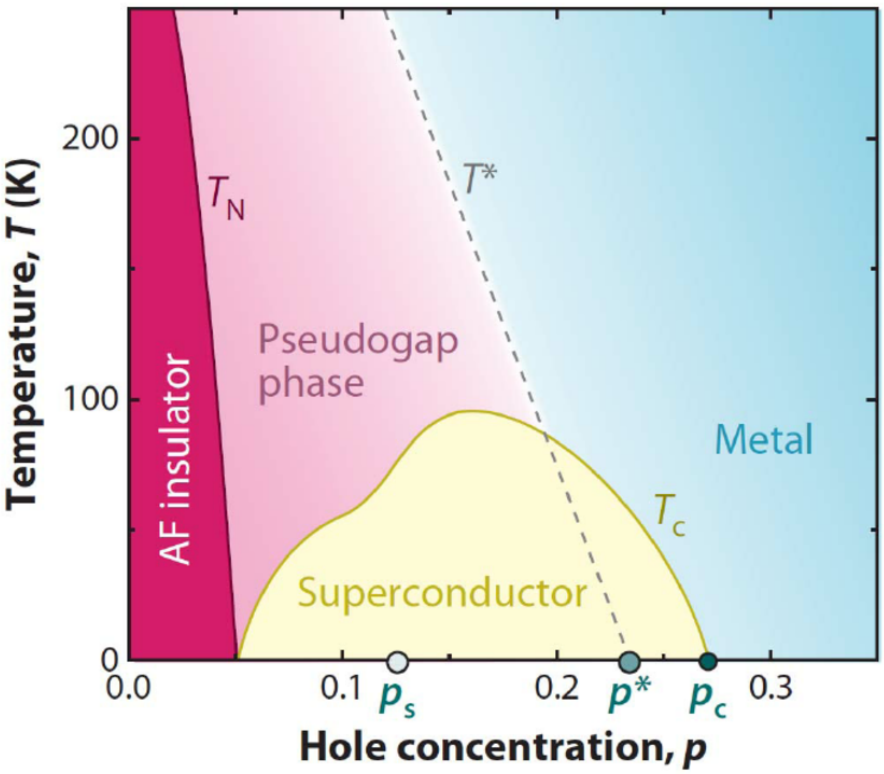

Figure 4-3*. The superconductor "dome" phase and the importance of doping (hole concentration) in high-temperature cuprates. In YBCO (*$YBa_2Cu_3O_{7-\delta}$*), when x=0 YBCO is an antiferromagnetic Mott insulator. When the ideal hole concentration is reached and YBCO is below the* T_c*, YBCO enters the superconducting phase.*

In the second trial, the Pymatgen (**Py**thon **Mat**erials **Gen**ome) Library was used to process doped unit cells into supercells with explicitly defined atomic species. Each supercell was created by repeating the unit cell a minimum number of times to include one dopant. An expanded supercell input removed all fractional sites from the input data. Supercells also emphasize the anisotropic, planar geometry found in known high-temperature superconductors. This allowed the retention of nearly all doped input files. A dataset of all high-temperature superconductors ($T_c > 45$ K) was used, including 400+ input files from cuprates, nickelates, and iron-based superconductors.

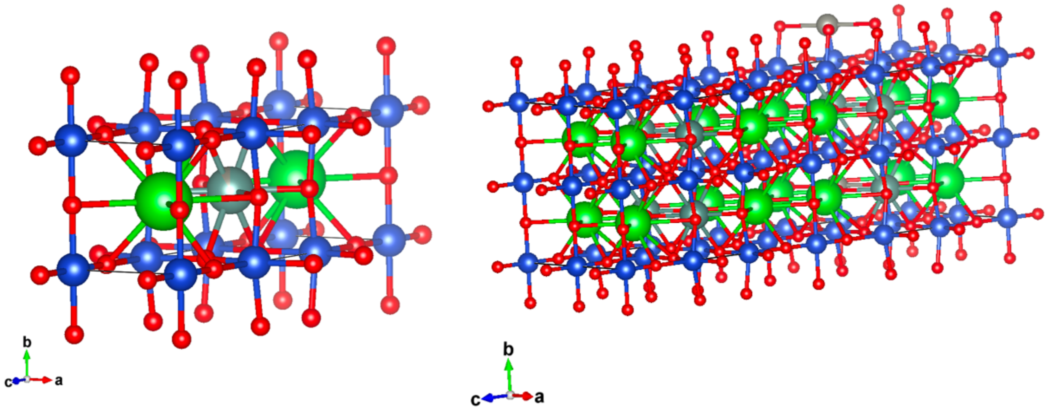

Figure 4-4. *YBCO doped with Zn. Left, unit cell with fractional site (Y0.9Zn0.1). Right, unit supercell with expanded sites (Y9Z1)…*

From these two trials, resulting structures were screened using ALIGNN (Atomistic Line Graph Neural Network), a graph-based model capable of capturing local bonding environments and geometric dependencies. ALIGNN was applied to predict material properties across various candidate supercells, including formation energy and band gap. Candidates with estimated formation energy < -0.5eV/atom were kept assessing stability. Band gap was also important in determining the viability of samples. For instance, iron-based parent compounds are metallic, while nickel- and copper-based superconductors are often antiferromagnetic insulators. DFT calculations are ideal for accurately screening candidates' electronic properties, providing access to more resources.

A simple optimization python script was used to manually tune output formulas to a target copper-oxidation state.

Datasets Used

Training data was sourced from the 3D Superconductor (3DSC) database[67]. 3DSC sources CIF files from ICSD[35], an experimentally determined crystal database. Theoretical structures were not included in training. Corresponding critical temperatures were listed in a comma separated variable (CSV) file for each superconductor CIF file, and provided as input to train CDVAE.

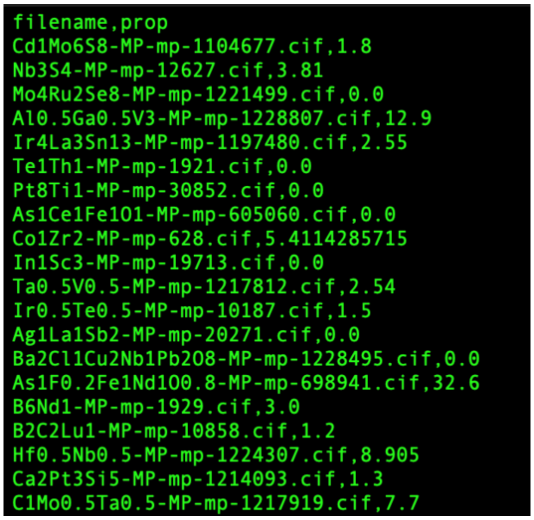

```
filename,prop
Cd1Mo6S8-MP-mp-1104677.cif,1.8
Nb3S4-MP-mp-12627.cif,3.81
Mo4Ru2Se8-MP-mp-1221499.cif,0.0
Al0.5Ga0.5V3-MP-mp-1228807.cif,12.9
Ir4La3Sn13-MP-mp-1197480.cif,2.55
Te1Th1-MP-mp-1921.cif,0.0
Pt8Ti1-MP-mp-30852.cif,0.0
As1Ce1Fe1O1-MP-mp-605060.cif,0.0
Co1Zr2-MP-mp-628.cif,5.4114285715
In1Sc3-MP-mp-19713.cif,0.0
Ta0.5V0.5-MP-mp-1217812.cif,2.54
Ir0.5Te0.5-MP-mp-10187.cif,1.5
Ag1La1Sb2-MP-mp-20271.cif,0.0
Ba2Cl1Cu2Nb1Pb2O8-MP-mp-1228495.cif,0.0
As1F0.2Fe1Nd1O0.8-MP-mp-698941.cif,32.6
B6Nd1-MP-mp-1929.cif,3.0
B2C2Lu1-MP-mp-10858.cif,1.2
Hf0.5Nb0.5-MP-mp-1224307.cif,8.905
Ca2Pt3Si5-MP-mp-1214093.cif,1.3
C1Mo0.5Ta0.5-MP-mp-1217919.cif,7.7
```

Figure 4-5*. Material ID property CSV file, featuring two columns: filename of the material ID, and the value of the property (critical temperature). This is used to map a directory of CIF files to corresponding critical temperatures for training the ALIGNN model.*

Training data was filtered into sub-datasets by composition to analyze critical temperature distribution of different structural families. Our total dataset of all compiled superconductors totaled 8865 crystals. The sub-datasets we defined were cuprates (copper oxides), iron-based, nickelates (nickel-based), palladites (palladium-based), and pure element superconductors. The training dataset used was a dataset of high-temperature compounds created by filtering the 3DSC dataset for materials with $T_c > 45K$.

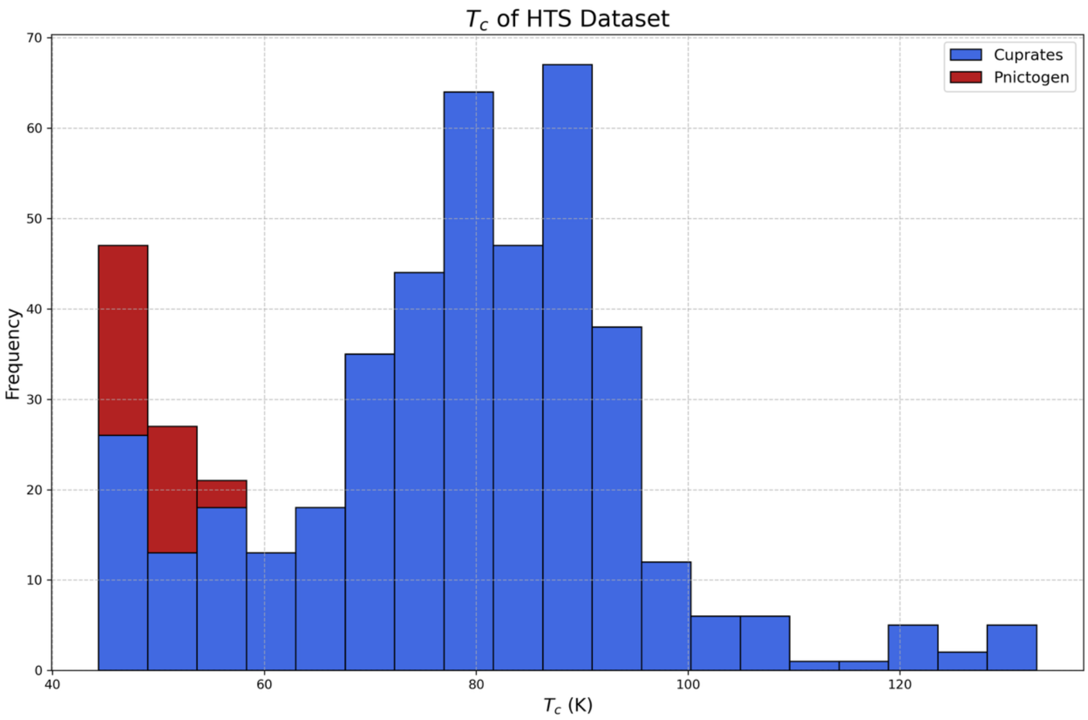

Figure 4-6. *A histogram showing the distribution of materials by their critical temperatures (T_c) in the high-temperature superconductor dataset employed in training CDVAE. Iron pnictogens and cuprate families composed the highest temperature datapoints.*

Experimental Validation

Laboratory Setup

Laboratory equipment used to synthesize polycrystalline superconductor pellets included Furnace 1: a Blue M Lab-Heat Muffle Furnace capable of temperatures over 1000 °C and a hydraulic press capable of over 10 tons of pressure. The effectiveness of lab equipment was benchmarked on the formation of $YBa_2Cu_3O_{7-\delta}$ samples by a solid-state reaction method before synthesizing new compounds. A meltdown malfunction occurred with Furnace 1, which was replaced by Furnace 2: a kiln sourced from the university sculpting department.

General Procedure

A solid-state reaction mechanism was used to synthesize polycrystalline ceramic pellets of candidate materials. Stoichiometric quantities of precursor oxides and carbonates were measured according to the target composition. Powders were milled in a porcelain mortar and pestle for 10 minutes until a homogenous powder was obtained. The mixture was transferred into a 13 mm hydraulic press die and compressed under 10 tons of pressure for 10 minutes to form a dense pellet. The pellet was calcinated in a porcelain dish at a temperature 950 ˚C for 24 hours.

The pellet was reanealled: cooled, milled into a fine powder, and pelletized a second time. This new pellet was sintered at temperature 950 ˚C for 24 hours. A precise cooling process began after the duration of 950 ˚C, cooling the pellet in the furnace at a rate of -100˚C/hour to 300˚C, then cooled to room temperature naturally. This thermal treatment tunes the oxygen content, δ, allowing oxygen to diffuse into the lattice. This is critical for stabilizing the superconductor phase.

The exception to this procedure were Bismuth-based ceramics, which were annealed at 850 ˚C.

Candidates Synthesized

The candidates synthesized were theorized from the described workflow. YBCO was used as a benchmark for our equipment. All other candidates were theoretical and synthesized by a solid-state reaction method.

Target Compound	**Starting Materials**
$YBa_2Cu_3O_{7-x}$	Y_2O_3, $BaCO_3$, CuO

$SrBa_2Cu_2O_{19}$	SrO, $BaCO_3$, CuO
$SrBa_2Cu_3O_{19}$	SrO, $BaCO_3$, CuO
$SrBa_2Cu_5O_{19}$	SrO, $BaCO_3$, CuO
$LaBa_2Cu_3O_y$	La2O3, $BaCO_3$, CuO
$YLaBa_4Cu_6O_{10}$	Y_2O_3, La_2O_3, $BaCO_3$, CuO
$YLaBa_2Sr_2Cu_6O_{16}$	Y_2O_3, La_2O_3, $BaCO_3$, SrO, CuO
$CeCu(I)Cu(II)O_4$	CeO_2, Cu2O, CuO
$Ce_{0.66}Cu(I)_{0.33}Ba_2Cu(II)_3O_{9-x}$	CeO_2, $BaCO_3$, Cu2O, CuO
$Ce_{0.5}Sr_{0.5}Ba_2Cu_3O_y$	CeO_2, SrO, CuO, $BaCO_3$
$Ce_{0.5}Sr_{0.5}Ba_2Cu_3O_y$	Y_2O_3, $BaCO_3$, CuO
$Bi_{9.5}Sr_{12}Ca_3Cu_5O_{34.25}$	$(BiO)_2CO_3$, SrO, CaO, CuO

Cerium Oxide (CeO_2) Synthesis

To synthesize cerium oxide for use in cerium-based superconductor candidates, a precipitation method was employed:

$$Ce^{4+}\ (aq) + 4\ OH^{-}\ (aq) \rightarrow CeO_2\ (s) + 2\ H_2O\ (l)$$

Ceric Ammonium Nitrate (CAN, 10.0 g) was dissolved in 100 mL of deionized water in a 250 mL beaker. Sodium hydroxide (4.4 g) was dissolved in 50 mL of deionized water in a 150 mL beaker. The NaOH solution was slowly added to the CAN solution under constant stirring, resulting in the formation of a precipitate. The resulting cerium oxide was isolated by vacuum filtration and subsequently washed with deionized water followed by acetone to remove residual impurities.

Superconductivity Determination

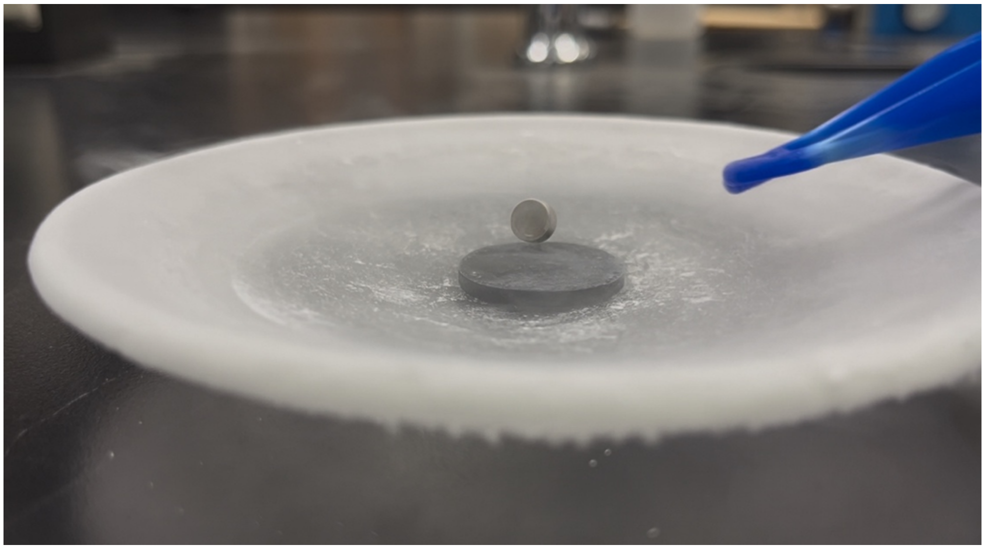

***Figure 4-7**. Meissner Effect for a YBCO pellet sample. When cooled below the critical temperature (T_c), YBCO enters the superconducting phase. For high-temperature superconductors, with $T_c > 77$ K (i.e., YBCO, Bi-2212, etc.) these temperatures can be reached with liquid nitrogen cooling.*

To assess the onset of superconductivity, the Meissner effect was used as a qualitative and semi-quantitative diagnostic. The Meissner effect (*Figure 1-1*) refers to the expulsion of magnetic flux from the interior of a superconductor upon its transition below the critical temperature (T_c). In practice, this effect enables a small permanent magnet to levitate above a superconducting material due to the formation of induced surface currents that oppose the applied magnetic field.

In this study, samples were cooled below 77 K using liquid nitrogen. Successful superconducting candidates exhibited stable magnetic levitation of neodymium magnets, indicating zero magnetic permeability and the establishment of a superconducting phase. To quantify levitation performance, a Levitation Percent Capacity (LPC) metric was defined as the ratio of the superconductor pellet mass to the mass of the magnet levitated:

$$LPC = \frac{m_{sample}}{m_{magnet}}$$

Higher LPC values suggest stronger magnetic exclusion and mechanical stability of the superconducting phase. This metric was used to tabulate and compare different synthesized compositions.

Sample	**Mass Levitated (g)**	**Pellet Mass (g)**	**LPC (%)**
1	0	5.177	0
1	0	4.856	0
1	0	5.018	0
2	2.156	5.961	36.17
2	1.716	5.960	28.79
3	0	7.669	0
4	2.467	7.347	33.58
5	0	8.770	0
6	4.290	5.170	82.98

***Table 2**. Recorded maximum mass levitation for six batch trials of synthesized YBCO samples, testing different annealing temperatures and cooling durations. The best performance was for sample 6. This was used to develop our general procedure.*

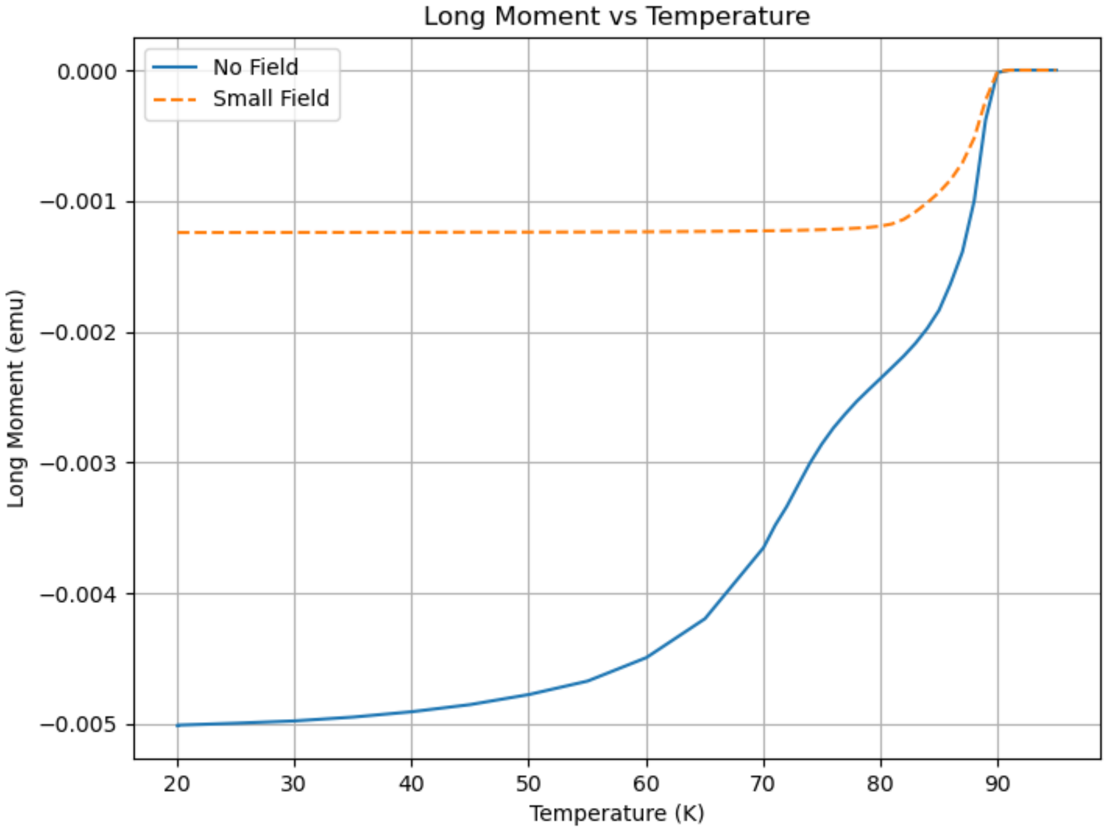

Figure 4-8. *Temperature vs. magnetic moment chart for measuring the critical temperature of a YBCO. Sourced from MPMS at Brookhaven National Laboratory.*

One YBCO sample was measured for exact critical temperature at Brookhaven National Laboratory via SQUID magnetometry with a recorded T_c = 91 K. Critical temperature determination of YBCO sample was performed using a Magnetic Properties Measurement System (MPMS). The MPMS measures the magnetic moment response as a function of temperature. Since the sample—if superconducting—becomes diamagnetic via the Meissner Effect upon reaching its critical temperature, it will expel external magnetic fields.

Thus, the sample's critical temperature can be identified as the point where the magnetic moment goes to zero. A second trial was performed under a small magnetic field of 10 Gauss. Magnetic fields can decrease the critical temperature of the sample. The MPMS records data in

CGS (centimeter-gram-second) units—the magnetic moment is measured in electromagnetic units (emu).

Oxygen Content Determination

Iodometry was used to determine the oxygen content of the copper oxide samples. A powdered $YBa_2Cu_3O_{7-\delta}$ (YBCO) sample was weighed (~300 mg) and dissolved in an Erlenmeyer flask in 10 mL of 6 M HCl, producing a yellow color. A solution of sodium iodide was prepared by adding 0.5 g of NaI into 20 mL of deionized water to form a 5% NaI solution. The NaI solution (10 mL) was added to the reaction flask, yielding a brown color. A starch solution (1%, five drops) was added while stirring, producing a blue-black color. The reaction solution was titrated with 0.01 M $Na_2S_2O_3$ until the blue-black color fades to clear. The initial and final burette volumes were recorded to determine the volume used.

Dissolving the sample in 6 M HCl releases Cu^{2+} and Cu^{3+} ions into the solution. Adding NaI causes the Cu^{3+} ions to oxidize I^- to I_2, reducing Cu^{3+} to Cu^{2+}:

$$2\mathrm{Cu}^{3+} + 2\mathrm{I}^- \rightarrow 2\mathrm{Cu}^{2+} + \mathrm{I}_2$$

The I_2 gives the solution a brown color. The starch solution forms a blue-black colored complex with I_2, making small amount visually detectable. The endpoint of the titration is marked by the blue-black color dissipating to clear. Thiosulfate reduces I_2 back to iodide:

$$\mathrm{I}_2 + 2\mathrm{S}_2\mathrm{O}_3^{2-} \rightarrow 2\mathrm{I}^- + \mathrm{S}_4\mathrm{O}_6^{2-}$$

The amount of $Na_2S_2O_3$ used corresponds stoichiometrically to the amount of Cu^{3+} present in the sample. Using the volume of thiosulfate used, the moles of $Na_2S_2O_3$ were determined to find the moles of Cu^{3+} as:

$$n_{Cu^{3+}} = n_{S_2O_3^{2-}}$$

2 $Cu^{3+} \rightarrow 1\ I_2 \rightarrow 2S_2O_3^{2-}$, so the ratio of Cu^{3+} to thiosulfate is 1:1. The sample mass of YBCO were used to find the total moles of Cu. The average Cu oxidation state, $\bar{x}$, was then solves as:

$$\bar{x} = \frac{n_{\mathrm{Cu}^{3+}} + 2n_{\mathrm{Cu,total}}}{n_{\mathrm{Cu,total}}}$$

Assuming charge neutrality, with Y^{3+}, Ba^{2+}, $\bar{x}$ for Cu, and O^{2-}, the oxygen content can be solved for algebraically as:

$$n_O = \frac{7 + 3\bar{x}}{2}$$

And used to solve for δ in the formula $YBa_2Cu_3O_{7-\delta}$ as:

$$\delta = 7 - n_O$$

Sample	Mass (mg)	$\bar{x}$	δ
1	339	2.020	0.468
2	310	2.021	0.470
3	308	2.018	0.473

Figure 4-9. *Oxygen content determined by iodometry for a superconducting YBCO sample. These values match with expectations from literature.*[68]

Magnetic Response

Gouy's method was employed to assess the magnetic behavior of synthesized samples under both ambient and cryogenic conditions. In this technique, powdered samples contained in test tubes were incrementally lowered toward a neodymium-alloy magnet placed on a precision balance. Any change in apparent magnet mass was recorded as an indicator of magnetic susceptibility. At room temperature, all samples exhibited weak paramagnetic responses, which became more pronounced upon cooling with liquid nitrogen. The $YBa_2Cu_3O_{7-x}$ (YBCO) benchmark sample deviated from this trend, demonstrating a clear diamagnetic response below its superconducting transition temperature—consistent with the onset of the Meissner effect.

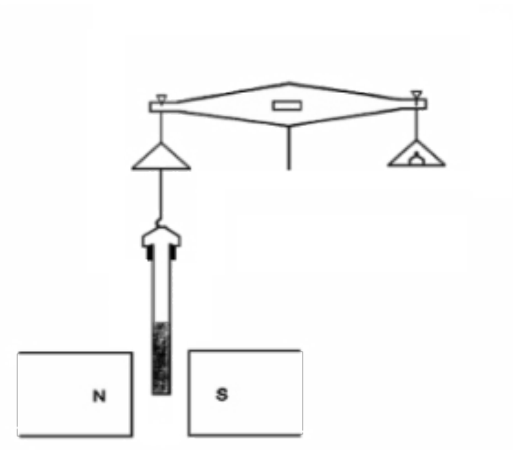

Figure 4-10. *Schematic for a Gouy balance. Powdered sample is lowered near a magnet and the change in mass is measured.*

Chapter 5 – Flow Past Cylinder Theory

We propose that superconductivity can be modeled as a special class of coherent fluid flow, where electron wavefunctions form vortical structures. Under the right conditions—analgous to fluid eddy merging—these defects annihilate or unify into a macroscopically coherent quantum state: the superconducting condensate.

Superconductivity is traditionally modeled using the BCS theory and Ginzburg-Landau (GL) phenomenology. These frameworks describe the formation of a macroscopic quantum state via Cooper pairing and phase coherence. However, the GL order parameter:

$$\psi(\boldsymbol{r}) = \sqrt{n(\boldsymbol{r})}e^{i\Phi}$$

Notably resembles the wavefunction of a quantum fluid. Here, $n(\boldsymbol{r})$ is the Cooper pair density, and $\phi\ (r)$ is the superconducting phase. This suggests a powerful analogy with classical vortex dynamics and coherent fluid motion. Further, the superconducting supercurrent velocity is directly tied to the phase gradient via:

$$\boldsymbol{J}_s = \frac{\hbar}{2m_e}\boldsymbol{\nabla}\phi$$

This is analogous to the velocity of an irrotational fluid:

$$\boldsymbol{v} = \boldsymbol{\nabla}\phi$$

Where ϕ is the velocity potential.

We attempt to create an analogy to fluid vortex dynamics. The model upholds: treating electrons as localized wave packets with spin and momentum; Cooper pairing is modeled as a form of vortex unification or annihilation; the superconducting state emerges from the coherence of eddy-like quantum flows; phase coherence is analogous to fluid coherence in low-viscosity fluids.

To illustrate this, we examine the dynamics of vortex merging in a 2D quantum fluid analog. We first examined the problem of merging vortices with opposite circulation. A 2D periodic domain is defined on a uniform grid with $x, y \in [-\mathrm{L}/2, \mathrm{L}/2]$. The vorticity of two Lamb-Oseen vortexes with equal and opposite circulation (representing spin, so this must be the case to obey the Pauli-Exclusion Principle), one centered at x = -1.5 with circulation Γ and the other at x=1.5 with circulation $-\Gamma$, can be described by:

$$\omega(x, y) = \frac{\Gamma}{\pi\sigma^2}e^{-r_1^2/\sigma^2} - \frac{\Gamma}{\pi\sigma^2}e^{-r_2^2/\sigma^2}$$

Where σ is the vortex core radius. Poisson's equation is solved to compute the stream function, ψ, as:

$$\boldsymbol{\nabla}^2\psi = -\omega(x, y),$$

From which the velocity field is obtained as:

$$v(x, y) = \boldsymbol{\nabla}^{\perp}\psi = \left(-\frac{\partial\psi}{\partial y}, \frac{\partial\psi}{\partial x}\right)$$

The velocity field governs the advection—or bulk flow—of vortical structures, and the merging dynamics represent phase-coherent condensation. This is akin to the collective alignment of quantum phases in a superconductor below T_c. Here is the evolution of two opposite spin vortices at long enough time step, from two incoherent vortices into a uniform stream, the basis of our argument that two disordered states can cohere into one.

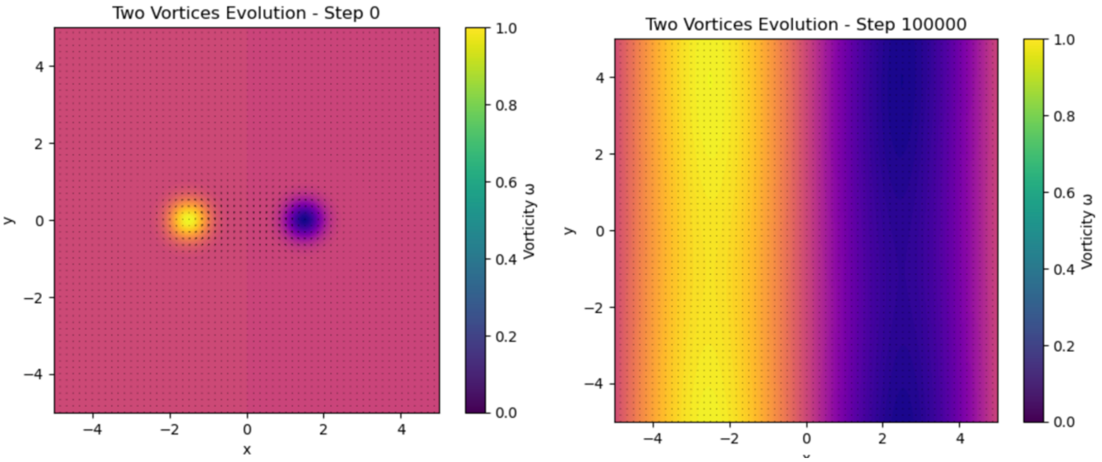

Figure 5-1: *Navier-Stokes simulation of the evolution of a vortex-anti-vortex pair evolving over time.* ***Left****: one vortex circulating clockwise, and another vortex circulating counterclockwise at time t = 0.* ***Right****: the resulting streams from the two vortices cancelling out the flows of the other pair. This simple problem was explored as an analogy to Cooper pair formation: two bound electrons with opposing spin forming a coherent quantum wavefunction.*

Future Work

This preliminary study introduces a hydrodynamic analogy for superconductivity in which Cooper pair formation is modeled as a form of vortex merging within a quantum fluid. By simulating the interaction of oppositely signed Lamb–Oseen vortices in a 2D domain, we have demonstrated that localized phase-defect structures—analogous to quantized vortices—can evolve into a coherent flow field. This transition parallels the onset of global phase coherence, and zero resistance observed in superconducting states. In future work, we will delve deeper into simulations and a theoretical derivation. This review outlines the general direction of this theory.

Chapter 6 – Conclusion & Outlook

Since there is no existing theory explaining the physics of high-temperature superconductors, a workflow is employed using machine learning, generative AI, and experimental validation to search for new materials. The proposed method—from data acquisition to structure generation, computational screening, and synthesis—successfully integrates theory, computation, and hands-on experimentation. Our results establish a foundation for a closed-loop discovery process. The integration of feedback from synthesis into the model retraining process can accelerate the design of materials beyond the capabilities of traditional trial-and-error methods. This work provides a roadmap for future research at the intersection of condensed matter physics, computational materials science, and AI, and emphasizes the importance of interdisciplinary approaches in tackling complex physical phenomena like high-T_c superconductivity.

Chapter 7 – Appendix

3DSC – 3D Superconductor Database: A machine-learning-ready dataset of known superconductors and their critical temperatures, used for training generative and predictive models.

AI – Artificial Intelligence: A broad field of computer science focused on building systems capable of tasks that typically require human intelligence, such as learning, reasoning, and pattern recognition.

ALIGNN – Atomistic Line Graph Neural Network: A graph neural network architecture that incorporates bond angles and higher-order interactions for accurate prediction of material properties.

Bi-based superconductors – Bismuth-based high-temperature superconductors, such as $Bi_2Sr_2CaCu_2O_{8+\delta}$ (Bi-2201 for $n = 1$, Bi-2212 for $n = 2$, Bi-2223 for $n = 3$), known for their layered structure and high T_c values. Where n is the number of CuO_2 layers.

CDVAE – Crystal Diffusion Variational Autoencoder: A generative model for creating novel crystal structures by learning the distribution of existing materials in latent space.

CGCNN – Crystal Graph Convolutional Neural Network: A graph-based model for predicting properties of crystalline materials by representing atoms as nodes and bonds as edges.

CIF – Crystallographic Information File: A standard file format for representing crystallographic structures, including atomic positions, symmetry, and lattice parameters.

CSV – Comma-Separated Values: A simple text-based file format used to store tabular data, often used for storing model outputs and training datasets.

DFT – Density Functional Theory: A quantum mechanical computational method used to study the electronic structure of materials.

Hg-based superconductors – Mercury-based high-Tc superconductors, such as $HgBa_2CaCu_2O_{6+\delta}$ (Hg-1201 for $n = 1$, Hg-1211 for $n = 2$, Hg-1223 for $n = 3$), known for achieving some of the highest T_c values at ambient pressure. Where n is the number of CuO_2 layers.

ICSD – Inorganic Crystal Structure Database: A comprehensive database of experimentally determined inorganic crystal structures used as reference data for materials discovery.

λ – London penetration depth: Characteristic length scale for magnetic field decay in a superconductor.

Λ - a dimensionless constant used in the London Equations:

$$\Lambda = \frac{4\pi\lambda^2}{c^2} = \frac{m}{n_s e^2}$$

Where λ, is the London penetration depth, n_s is the density of superconducting electrons, c is the speed of light, e is the elementary charge of an electron, and m is the mass of an electron.

LBCO – $La_{2-x}Ba_xCuO_4$: A cuprate superconductor exhibiting stripe order and complex electronic behavior, often used in doping studies.

LSCO – $La_{2-x}Sr_xCuO_4$: A prototypical single-layer cuprate used to study the doping dependence of superconductivity and magnetism.

ML – Machine Learning: A subset of AI focused on algorithms that allow computers to learn patterns and make decisions from data without being explicitly programmed.

T_c – Critical Temperature: The temperature below which a material exhibits zero electrical resistance and expels magnetic fields (the Meissner effect), entering the superconducting state.

Tl-based superconductors – Thallium-based cuprates, such as $Tl_2Ba_2CaCu_2O_{8+\delta}$ (Tl-2201 for $n = 1$, Tl-2212 for $n = 2$, Tl-2223 for $n = 3$), known for their high T_c and layered crystal structure. Where n is the number of CuO_2 layers.

VAE – Variational Autoencoder: A type of generative neural network that learns a probability distribution over latent representations of data, allowing for the generation of new samples.

XRD – X-ray Diffraction: An experimental technique used to determine the crystal structure of materials by measuring the diffraction pattern of X-rays passing through the sample.

YBCO – $YBa_2Cu_3O_{7-\delta}$: A well-known high- T_c cuprate superconductor with an orthorhombic perovskite structure, notable for its relatively low anisotropy and use in practical applications.

Chapter 8 – Acknowledgments

First and foremost, I would like to thank Dr. Ivan Fabe Dempsey Hyatt for his support in this project. Without the last 4 years of his guidance through scientific research, my ambition to work towards discovering new superconductors would not have been fostered.

I would also like to thank Dr. Matthew Wright for his help in guiding my thesis in Fall 2024, and for guiding my academic career in physics.

An additional special thank you to Dr. Niraj Aryal for introducing me to graph neural networks and computational materials science techniques during two summer internships in the Condensed Matter Department at Brookhaven National Laboratory.

Additional acknowledgments go out to Dr. Qiang Li, Sarah, and Juntao for allowing me to perform MPMS measurements on YBCO samples at Brookhaven National Laboratory.

And a final, special thank you to Dean Nicole Rudolph of the Honors College for guiding the honors thesis project.

Chapter 9 - References

(1) Van Delft, D.; Kes, P. The Discovery of Superconductivity. *Phys Today* **2010**, *63* (9), 38–43. https://doi.org/10.1063/1.3490499.

(2) Michael Tinkham. *Introduction to Superconductivity: Second Edition*; Dover Publications: Garden City, **1996**.

(3) Bardeen, J.; Cooper, L. N.; Schrieffer, J. R. *Theory of Superconductivity*. *Phys. Rev.* **1957**, *108*, 1175–1204. https://doi.org/10.1103/PhysRev.108.1175.

(4) Kramer, D. Helium Is Again in Short Supply. *Phys. Today* **2022**, *75* (5), 20–21. https://doi.org/10.1063/PT.3.5006.

(5) Bednorz, J. G.; Miiller, K. A. *Condensed Possible High Tc Superconductivity in the Ba-La-Cu-0 System*; **1986**; Vol. 64.

(6) Wu, M. K.; Ashburn, J. R.; Torng, C. J.; Hor, P. H.; Meng, R. L.; Gao, L.; Huang, Z. J.; Wang, Y. Q.; Chu ', C. W. *PHYSICAL REVIEW LETTERS Superconductivity at 93 K in a New Mixed-Phase Y-Ba-Cu-0 Compound System at Ambient Pressure*; **1987**; Vol. 58.

(7) Kramer, D. Helium Prices Surge to Record Levels as Shortage Continues. *Phys Today* **2023**, *76* (9), 18–20. https://doi.org/10.1063/PT.3.5305.

(8) Elishav, O.; Lewin, D. R.; Shter, G. E.; Grader, G. S. The Nitrogen Economy: Economic Feasibility Analysis of Nitrogen-Based Fuels as Energy Carriers. *Appl Energy* **2017**, *185*, 183–188. https://doi.org/10.1016/j.apenergy.2016.10.088.

(9) Bussmann-Holder, A.; Keller, H. High-Temperature Superconductors: Underlying Physics and Applications. *Zeitschrift fur Naturforschung - Section B Journal of Chemical Sciences* **2019**, 3–14. https://doi.org/10.1515/znb-2019-0103.

(10) *Field Dependence of the Vortex Structure in D-Wave and S-Wave Superconductors*. *Phys. Rev. B* **1999**, *59* (13), 8902–8916. https://doi.org/10.1103/PhysRevB.59.8902..

(11) Faber, T. E.; Pippard, A. B. The Penetration Depth and High-Frequency Resistance of Superconducting Aluminium. *Proc R Soc Lond A Math Phys Sci* **1955**.

(12) U.S. Congress, Office of Technology Assessment. *High-Temperature Superconductivity in Perspective*; OTA-E-440; U.S. Government Printing Office: Washington, DC, **1990**. https://www.princeton.edu/~ota/disk2/1990/9024/902405.PDF.

(13) Lee, H.-W.; Kim, K.-C.; Lee, J. *Review of Maglev Train Technologies*. *IEEE Trans. Magn.* **2006**, *42* (7), 1917–1925. https://doi.org/10.1109/TMAG.2006.875842.

(14) Yamamoto, A. *Superconducting Magnets Advanced in Particle Physics*; 2000; Vol. 453.

(15) Forsyth, E. B.; Mulligan, G. A.; Beck, J. W.; Williams, J. A. Technical and Economic Feasibility of Superconducting Power Transmission: A Case Study; IEEE Trans. Power Appar. Syst. **1975**, 94 (1), 161–170. https://doi.org/10.1109/TPAS.1975.32045.

(16) Brookhaven National Laboratory. *Relativistic Heavy Ion Collider (RHIC)*. https://www.bnl.gov/rhic/ (accessed May 11, 2025).

(17) Northeast Maglev. *The SCMAGLEV Project – Fastest Train in the World*. https://northeastmaglev.com/project/ (accessed May 9, 2025).

(18) Xiang, B.; Liu, Z.; Geng, Y.; Yanabu, S. DC Circuit Breaker Using Superconductor for Current Limiting. *IEEE Transactions on Applied Superconductivity* **2015**, *25* (2). https://doi.org/10.1109/TASC.2014.2363058.

(19) Pham, Q. H.; Noe, M.; Nast, R. *Resistance of High-Temperature Superconducting Tapes Triggered by Alternating Magnetic Field. IEEE Trans. Appl. Supercond.* **2025**, *35* (3), 1–5. https://doi.org/10.1109/TASC.2025.3550837.

(20) Clarke, J.; Alex I. Braginski. *The SQUID Handbook: Applications of SQUIDs and SQUID Systems*; John Wiley & Sons, **2006**.

(21) Grilli, F.; Benkel, T.; Hänisch, J.; Lao, M.; Reis, T.; Berberich, E.; Wolfstädter, S.; Schneider, C.; Miller, P.; Palmer, C.; Glowacki, B.; Climente-Alarcon, V.; Smara, A.; Tomkow, L.; Teigelkötter, J.; Stock, A.; Büdel, J.; Jeunesse, L.; Staempflin, M.; Delautre, G.; Zimmermann, B.; Van Der Woude, R.; Perez, A.; Samoilenkov, S.; Molodyk, A.; Pardo, E.; Kapolka, M.; Li, S.; Dadhich, A. *Superconducting Motors for Aircraft Propulsion: The Advanced Superconducting Motor Experimental Demonstrator Project. J. Phys.: Conf. Ser.* **2020**, *1590*, 012051. https://doi.org/10.1088/1742-6596/1590/1/012051.

(22) Questions and Answers in MRI. https://mriquestions.com/ (accessed May 11, 2025).

(23) Manso Jimeno, M.; Vaughan, J. T.; Geethanath, S. Superconducting Magnet Designs and MRI Accessibility: A Review. NMR Biomed. **2023**, 36 (9), e4921. https://doi.org/10.1002/nbm.4921.

(24) *Superconducting Magnet for Medical MRI System Market. Verified Market Reports. https://www.verifiedmarketreports.com/product/superconducting-magnet-for-medical-mri-system-market/ (accessed May 11, 2025).*

(25) Merchant, A.; Batzner, S.; Schoenholz, S. S.; Aykol, M.; Cheon, G.; Cubuk, E. D. Scaling Deep Learning for Materials Discovery. *Nature* **2023**, *624* (7990), 80–85. https://doi.org/10.1038/s41586-023-06735-9.

(26) Pyzer-Knapp, E. O.; Pitera, J. W.; Staar, P. W. J.; Takeda, S.; Laino, T.; Sanders, D. P.; Sexton, J.; Smith, J. R.; Curioni, A. Accelerating Materials Discovery Using Artificial Intelligence, High Performance Computing and Robotics. *NPJ Comput Mater* **2022**, *8* (1). https://doi.org/10.1038/s41524-022-00765-z.

(27) Nematov, D.; Hojamberdiev, M. Machine Learning–Driven Materials Discovery: Unlocking Next-Generation Functional Materials—A Minireview. arXiv **2025**, arXiv:2503.18975. https://arxiv.org/abs/2503.18975.

(28) Xie, T.; Grossman, J. C. Crystal Graph Convolutional Neural Networks for an Accurate and Interpretable Prediction of Material Properties. *Phys Rev Lett* **2018**, *120* (14). https://doi.org/10.1103/PhysRevLett.120.145301.

(29) Merchant, A.; Batzner, S.; Schoenholz, S. S.; Aykol, M.; Cheon, G.; Cubuk, E. D. Scaling Deep Learning for Materials Discovery. *Nature* **2023**, *624* (7990), 80–85. https://doi.org/10.1038/s41586-023-06735-9.

(30) Wines, D.; Xie, T.; Choudhary, K. Inverse Design of Next-Generation Superconductors Using Data-Driven Deep Generative Models. **2023**. https://doi.org/10.1021/acs.jpclett.3c01260.

(31) Yazdani-Asrami, M.; Sadeghi, A.; Song, W.; Madureira, A.; Murta-Pina, J.; Morandi, A.; Parizh, M. Artificial Intelligence Methods for Applied Superconductivity: Material, Design, Manufacturing, Testing, Operation, and Condition Monitoring. *Superconductor Science and Technology*. Institute of Physics December 1, **2022**. https://doi.org/10.1088/1361-6668/ac80d8.

(32) Han, X.-Q.; Ouyang, Z.; Guo, P.-J.; Sun, H.; Gao, Z.-F.; Lu, Z.-Y. InvDesFlow: An AI Search Engine to Explore Possible High-Temperature Superconductors. **2024**.

(33) Tran, H.; Dam, H. C.; Kuenneth, C.; Ngoc Tuoc, V.; Kino, H. Superconductor Discovery in the Emerging Paradigm of Materials Informatics. *Chemistry of Materials*. American Chemical Society November 26, **2024**. https://doi.org/10.1021/acs.chemmater.4c01757.

(34) Jain, A.; Ong, S. P.; Hautier, G.; Chen, W.; Richards, W. D.; Dacek, S.; Cholia, S.; Gunter, D.; Skinner, D.; Ceder, G.; Persson, K. A. Commentary: The Materials Project: A Materials Genome Approach to Accelerating Materials Innovation. *APL Materials*. American Institute of Physics Inc. **2013**. https://doi.org/10.1063/1.4812323.

(35) Igor Levin. NIST Inorganic Crystal Structure Database (ICSD). **2018**.

(36) Chen, C.; Nguyen, D. T.; Lee, S. J.; Baker, N. A.; Karakoti, A. S.; Lauw, L.; Owen, C.; Mueller, K. T.; Bilodeau, B. A.; Murugesan, V.; Troyer, M. Accelerating Computational Materials Discovery with Machine Learning and Cloud High-Performance Computing: From Large-Scale Screening to Experimental Validation. *J Am Chem Soc* **2024**, *146* (29), 20009–20018. https://doi.org/10.1021/jacs.4c03849.

(37) Jha, D.; Gupta, V.; Liao, W. keng; Choudhary, A.; Agrawal, A. Moving Closer to Experimental Level Materials Property Prediction Using AI. *Sci Rep* **2022**, *12* (1). https://doi.org/10.1038/s41598-022-15816-0.

(38) Merchant, A.; Cubuk, E. D. *Millions of New Materials Discovered with Deep Learning*. DeepMind. https://deepmind.google/discover/blog/millions-of-new-materials-discovered-with-deep-learning/ (accessed May 11, 2025).

(39) Huang, X. A Unified Theory of Superconductivity. arXiv **2008**, arXiv:0804.1615. https://doi.org/10.48550/arXiv.0804.1615.

(40) Dynes, R. C. McMillan's Equation and the Tc of Superconductors. *Solid State Commun.* **1972**, *10* (8), 615–618. https://doi.org/10.1016/0038-1098(72)90603-5.

(41) Dahm, T.; Hinkov, V.; Borisenko, S. V.; Kordyuk, A. A.; Zabolotnyy, V. B.; Fink, J.; Büchner, B.; Scalapino, D. J.; Hanke, W.; Keimer, B. Strength of the Spin-Fluctuation-Mediated Pairing Interaction in a High-Temperature Superconductor. *Nat Phys* **2009**, *5* (3), 217–221. https://doi.org/10.1038/nphys1180.

(42) Plakida, N. M. Spin Fluctuations and High-Temperature Superconductivity in Cuprates. *Physica C: Superconductivity and its Applications*. Elsevier B.V. December 15, **2016**, pp 39–59. https://doi.org/10.1016/j.physc.2016.10.002.

(43) Nikolay Plakida. *High-Temperature Cuprate Superconductors: Experiment, Theory, and Applications*; **2010**.

(44) Nomura, Y.; Arita, R. Superconductivity in Infinite-Layer Nickelates. *Reports on Progress in Physics*. IOP Publishing Ltd May 1, **2022**. https://doi.org/10.1088/1361-6633/ac5a60.

(45) Stewart, G. R. Superconductivity in Iron Compounds. *Rev Mod Phys* **2011**, *83* (4). https://doi.org/10.1103/RevModPhys.83.1589.

(46) Boebinger, G. S.; Chubukov, A. V.; Fisher, I. R.; Grosche, F. M.; Hirschfeld, P. J.; Julian, S. R.; Keimer, B.; Kivelson, S. A.; Mackenzie, A. P.; Maeno, Y.; Orenstein, J.; Ramshaw, B. J.; Sachdev, S.; Schmalian, J.; Vojta, M. Hydride Superconductivity Is Here to Stay. *Nature Reviews Physics*. Springer Nature January 1, **2024**. https://doi.org/10.1038/s42254-024-00794-1.

(47) Barišić, N.; Chan, M. K.; Li, Y.; Yu, G.; Zhao, X.; Dressel, M.; Smontara, A.; Greven, M. Universal Sheet Resistance and Revised Phase Diagram of the Cuprate High-Temperature Superconductors. Proc. Natl. Acad. Sci. U.S.A. **2013**, 110 (30), 12235–12240. https://doi.org/10.1073/pnas.1301989110.

(48) Ray, Pia. Structural Investigation of La(2-x)Sr(x)CuO(4+y) - Following Staging as a Function of Temperature, **2015**.

(49) Jamet, F.; Weber, C.; Acharya, S.; Pashov, D.; Van Schilfgaarde, M. Disentangling the Role of Bond Lengths and Orbital Symmetries in Controlling Tc of Optimally Doped YBa2Cu3 O7. *Phys Rev Res* **2022**, *4* (3). https://doi.org/10.1103/PhysRevResearch.4.033189.

(50) Mariano, A. L.; Poloni, R. Electric Field-Induced Oxygen Vacancies in YBa2Cu3O7. *Journal of Chemical Physics* **2021**, *154* (22). https://doi.org/10.1063/5.0048597.

(51) Banerjee, S.; Atkinson, W. A.; Kampf, A. P. Emergent Charge Order from Correlated Electron-Phonon Physics in Cuprates. *Commun Phys* **2020**, *3* (1). https://doi.org/10.1038/s42005-020-00430-1.

(52) Shamray, V. F.; Mikhailova, A. B.; Mitin, A. V. Crystal Structure and Superconductivity of Bi-2223. *Crystallography Reports* **2009**, *54* (4), 584–590. https://doi.org/10.1134/S1063774509040075.

(53) Morosin, B.; Ginley, D. S.; Hlava, P. F.; Carr, M. J.; Baughman, R. J.; Schirber, J. E.; Venturini, E. L.; Kwak, J. F. Structural and Compositional Characterization of Polycrystals and Single Crystals in the Bi- and Tl-Superconductor Systems: Crystal Structure of $TlCaBa_2Cu_2O_7$. J. Less-Common Met. **1989**, 152, 1–12. https://doi.org/10.1016/0022-5088(89)90210-5.

(54) *Cuprate Superconductor. https://en.wikipedia.org/wiki/Cuprate_superconductor (accessed May 11, 2025).*

(55) Thomson, Stuart. Observing Phase Transitions in a Halide Perovskite Using Temperature Dependent Photoluminescence Spectroscopy. . **2018**.

(56) Hott, R. Materials Aspects of High-Temperature Superconductors for Applications. . **2003**.

(57) Raveau, B.; Michel, C.; Hervieu, M.; Maignan, A. *Crystal Chemistry of Superconducting Mercury-Based Cuprates and Oxycarbonates*; **1995**; Vol. 5.

(58) Kordyuk, A. A.; Borisenko, S. V. ARPES on High-Temperature Superconductors: Simplicity vs. Complexity (Review Article). *Low Temperature Physics*. American Institute of Physics Inc. **2006**, pp 298–304. https://doi.org/10.1063/1.2199429.

(59) Markiewicz, R. S.; Singh, B.; Lane, C.; Bansil, A. Investigating the Cuprates as a Platform for High-Order Van Hove Singularities and Flat-Band Physics. *Commun Phys* **2023**, *6* (1). https://doi.org/10.1038/s42005-023-01373-z.

(60) Halcrow, M. A. Jahn–Teller Distortions in Transition Metal Compounds, and Their Importance in Functional Molecular and Inorganic Materials. *Chem Soc Rev* **2013**, *42* (4), 1784–1795. https://doi.org/10.1039/c2cs35253b.

(61) Xie, T.; Fu, X.; Ganea, O.-E.; Barzilay, R.; Jaakkola, T. Crystal Diffusion Variational Autoencoder for Periodic Material Generation. **2021**.

(62) Du, W.; Zhang, H.; Du, Y.; Meng, Q.; Chen, W.; Shao, B.; Liu, T.-Y. SE(3) Equivariant Graph Neural Networks with Complete Local Frames. **2021**.

(63) Paquet, E.; Viktor, H. L. Molecular Dynamics, Monte Carlo Simulations, and Langevin Dynamics: A Computational Review. *BioMed Research International*. Hindawi Publishing Corporation **2015**. https://doi.org/10.1155/2015/183918.

(64) Chen, C.; Ong, S. P. A Universal Graph Deep Learning Interatomic Potential for the Periodic Table. *Nat Comput Sci* **2022**, *2* (11), 718–728. https://doi.org/10.1038/s43588-022-00349-3.

(65) Yang, Z.; Zhao, Y. M.; Wang, X.; Liu, X.; Zhang, X.; Li, Y.; Lv, Q.; Chen, C. Y. C.; Shen, L. Scalable Crystal Structure Relaxation Using an Iteration-Free Deep Generative Model with Uncertainty Quantification. *Nature Communications* **2024**, *15* (1). https://doi.org/10.1038/s41467-024-52378-3.

(66) Choudhary, K.; DeCost, B. Atomistic Line Graph Neural Network for Improved Materials Property Predictions. *NPJ Comput Mater* **2021**, *7* (1). https://doi.org/10.1038/s41524-021-00650-1.

(67) Sommer, T.; Willa, R.; Schmalian, J.; Friederich, P. 3DSC - a Dataset of Superconductors Including Crystal Structures. *Sci Data* **2023**, *10* (1). https://doi.org/10.1038/s41597-023-02721-y.

(68) Liu, L.; Dong, C.; Zhang, J.; Chen, H.; Chen, L. A Simple Volumetric Method for Oxygen Content Determination in High-Tc Doped YBCO Compositions. Physica C **2002**, 383 (1), 17–22. https://doi.org/10.1016/S0921-4534(02)01268-6.